

1 Application of the Multi-Scale Infrastructure for Chemistry and Aerosols 2 version 0 (MUSICAv0) for air quality research in Africa

3
4
5 Wenfu Tang¹, Louisa K. Emmons¹, Helen M. Worden¹, Rajesh Kumar², Cenlin He²,
6 Benjamin Gaubert¹, Zhonghua Zheng³, Simone Tilmes¹, Rebecca R. Buchholz¹, Sara-Eva
7 Martinez-Alonso¹, Claire Granier^{4,5}, Antonin Soulie⁴, Kathryn McKain⁶, Bruce C. Daube⁷,
8 Jeff Peischl^{5,8}, Chelsea Thompson⁸, and Pieter Levelt^{1,9,10}
9

10 ¹Atmospheric Chemistry Observations & Modeling Laboratory, National Center for Atmospheric
11 Research, Boulder, CO, USA

12 ²Research Applications Laboratory, National Center for Atmospheric Research, Boulder, CO,
13 USA

14 ³Department of Earth and Environmental Sciences, The University of Manchester, Manchester
15 M13 9PL, United Kingdom

16 ⁴Laboratoire d'Aérodynamique, CNRS, Université de Toulouse, Toulouse, France

17 ⁵Cooperative Institute for Research in Environmental Sciences (CIRES), University of Colorado,
18 Boulder, CO, USA

19 ⁶Global Monitoring Laboratory (GML), National Oceanic and Atmospheric Administration,
20 Boulder, CO, USA

21 ⁷Department of Earth and Planetary Sciences, Harvard University, Cambridge, MA, USA

22 ⁸NOAA Chemical Sciences Laboratory, Boulder, CO, USA

23 ⁹Royal Netherlands Meteorological Institute (KNMI), Utrechtseweg 297, 3730 AE De Bilt, the
24 Netherlands

25 ¹⁰University of Technology Delft, Mekelweg 5, 2628 CD Delft, the Netherlands
26

27 Correspondence: Wenfu Tang (wenfut@ucar.edu)
28
29

30 **Abstract**

31 The Multi-Scale Infrastructure for Chemistry and Aerosols Version 0 (MUSICAv0) is a new
32 community modeling infrastructure that enables the study of atmospheric composition and
33 chemistry across all relevant scales. We develop a MUSICAv0 grid with Africa refinement (~28
34 km × 28 km over Africa). We evaluate the MUSICAv0 simulation for 2017 with in situ
35 observations and compare the model results to satellite products over Africa. A simulation from
36 the Weather Research and Forecasting model coupled with Chemistry (WRF-Chem), a regional
37 model that is widely used in Africa studies, is also included in the analyses as a reference. Overall,
38 the performance of MUSICAv0 is comparable to WRF-Chem. Both models underestimate carbon
39 monoxide (CO) compared to in situ observations and satellite CO column retrievals from the
40 Measurements of Pollution in the Troposphere (MOPITT) satellite instrument. MUSICAv0 tends
41 to overestimate ozone (O₃), likely due to overestimated stratosphere-to-troposphere flux of ozone.
42 Both models significantly underestimate fine particulate matter (PM_{2.5}) at two surface sites in East
43 Africa. The MUSICAv0 simulation agrees better with aerosol optical depth (AOD) retrievals from
44 the Moderate Resolution Imaging Spectroradiometer (MODIS) and tropospheric nitrogen dioxide

45 (NO₂) column retrievals from the Ozone Monitoring Instrument (OMI) than WRF-Chem.
46 MUSICAv0 has a consistently lower tropospheric formaldehyde (HCHO) column than OMI
47 retrievals. Based on model-satellite discrepancies between MUSICAv0 and WRF-Chem and
48 MOPITT CO, MODIS AOD, and OMI tropospheric NO₂, we find that future field campaign(s)
49 and more in situ observations in an East African region (30°E – 45°E, 5°S – 5°N) could
50 substantially improve the predictive skill of atmospheric chemistry model(s). This suggested focus
51 region exhibits the largest model-in situ observation discrepancies, as well as targets for high
52 population density, land cover variability, and anthropogenic pollution sources.

53

54 **1. Introduction**

55 As one of the most dramatically changing continents, Africa is experiencing myriad
56 environmental sustainability issues (e.g., Davidson et al., 2003; Washington et al., 2006; Ziervogel
57 et al., 2014; Boone et al., 2016; Swilling et al., 2016; Baudoin et al., 2017; Güneralp et al., 2017;
58 Nicholson 2019; Fisher et al., 2021; Langerman et al., 2023). These environmental issues are
59 causing vast losses in lives and in African economies, and are coupled with poverty and under-
60 development (Washington et al., 2006; Fisher et al., 2021). Some of these environmental
61 challenges are particularly severe in Africa compared to many other regions of the world (e.g.,
62 droughts, floods, high temperatures, land degradation, and fires; Washington et al., 2006; Nka et
63 al., 2015; van der Werf et al., 2017; Haile et al., 2019). However, even though Africa is the second
64 largest continent, in land area and population, attention and research on environmental challenges
65 in Africa are very limited, leading to a deficit of knowledge and solutions (e.g., De Longueville et
66 al., 2010). Intergovernmental Panel on Climate Change (IPCC) computes a human vulnerability
67 metric from existing challenges such as poverty, access to health care plus expected mortality for
68 climate hazards such as heat, drought, flood, fires and constraints to adaptation like funding, and
69 government infrastructure (Moss et al., 2001). Many regions in Africa exhibit the most extreme
70 values for this metric.

71 Degraded air quality is an example of a severe environmental challenge with growing
72 importance in Africa (e.g., Kinney et al., 2011; Naiker et al., 2012; Liousse et al., 2014; Thompson
73 et al., 2014; Amegah et al., 2017; Heft-Neal et al., 2018; Fisher et al., 2021; Okure et al., 2022;
74 Vohra et al., 2022). A previous study found that air pollution across Africa caused ~1.1 million
75 deaths in 2019 (Fisher et al., 2021). However, the study of air quality in Africa is hindered by the
76 scarcity of ground-based observations (e.g., Paton-Walsh et al., 2022; Kalisa et al., 2023),
77 modelling capability and the use of satellite observations. In this paper, we will focus on air quality
78 analyses over Africa with the new model Multi-Scale Infrastructure for Chemistry and Aerosols
79 (MUSICA; Pfister et al., 2020).

80 Atmospheric chemistry modeling is a useful tool to provide air quality forecasts and to
81 understand chemical processes. Various models have been applied to study atmospheric chemistry
82 and air quality in Africa such as the Weather Research and Forecasting (WRF) model coupled with
83 Chemistry (WRF-Chem) (e.g., Kuik et al., 2015; Kumar et al., 2022; Jenkins and Gueye, 2022),
84 the GEOS-Chem chemical transport model (e.g., Marais et al., 2012, 2019; Lacey et al., 2018), the
85 CHIMERE chemical transport model (e.g., Menut et al., 2018; Mazzeo et al., 2022), and the U.K.
86 Earth System Model (UKESM1) (Brown et al., 2022), and GEOS5 (Bauer et al., 2019).

87 MUSICA is a new state-of-the-art community modeling infrastructure that enables the
88 study of atmospheric composition and chemistry across all relevant scales (Pfister et al., 2020).
89 The newly developed MUSICA Version 0 (MUSICAv0) is a global chemistry-climate model that
90 allows global simulations with regional refinement down to a few kilometers spatial resolution

91 (Schwantes et al., 2022). The coupling with other components of the Earth system (e.g., land,
92 ocean, and sea ice) can also be performed at multiple scales. MUSICAv0 has various advantages
93 and is particularly suitable for research applications over Africa. For example, MUSICAv0 can be
94 used to study the interactions between atmospheric chemistry and other components of the Earth
95 system and climate. MUSICAv0 also includes the whole atmosphere (from the surface to
96 thermosphere), and therefore can also be used to study the stratosphere and above and interactions
97 between the stratosphere and troposphere. This is critical because some of the environmental issues
98 are coupled (e.g., the ozone–climate penalty; Brown et al., 2022). In addition, as a global model,
99 MUSICAv0 does not require boundary conditions to study a region at high resolution. Global
100 impacts and interactions can be simulated in a consistent and coherent way. This feature is
101 important as inflow from other continents and oceans significantly impacts air quality in Africa.
102 MUSICAv0 has been evaluated over North America (Schwantes et al., 2022, Tang et al., 2022)
103 and is also being developed and tested in other regions around the globe
104 (<https://wiki.ucar.edu/display/MUSICA/Available+Grids>).

105 This paper serves as the basis for the future application of MUSICAv0 in Africa. In this
106 study, we develop a MUSICAv0 model grid with regional refinement over Africa. Because
107 MUSICAv0 with Africa refinement is newly developed while WRF-Chem has been previously
108 used for African atmospheric chemistry and air quality studies, here we include results from WRF-
109 Chem to assess the ability of MUSICAv0 in reproducing the regional features of atmospheric
110 composition as simulated by WRF-Chem. We conduct the MUSICAv0 simulation for the year
111 2017 to compare with a previous WRF-Chem simulation (Kumar et al., 2022). MUSICAv0 and
112 the WRF-Chem simulation and the observational data used in this study are described in Section
113 2. The MUSICAv0 model simulation results are evaluated against in situ observations and
114 compared with satellite retrievals in Section 3. In Section 4, we provide an example application of
115 MUSICAv0 over Africa – identifying key potential regions in Africa for future in situ observations
116 and field campaign(s).

117

118 **2. Model and data**

119 **2.1 MUSICAv0**

120 MUSICAv0 is a newly developed framework for simulations of large-scale atmospheric
121 phenomena in a global modeling framework, while still resolving chemistry at emission- and
122 exposure-relevant scales (Pfister et al., 2020). MUSICAv0 is a configuration
123 of the Community Earth System Model (CESM). It is also known as the Community Atmospheric
124 Model with chemistry (CAM-chem) (Tilmes et al., 2019; Emmons et al., 2020) with regional
125 refinement (RR) down to a few kilometers (Lauritzen et al., 2018; Schwantes et al., 2022). CAM-
126 chem, and thus MUSICAv0, includes several choices of chemical mechanisms of varying
127 complexity. This study uses the default MOZART-TS1 chemical mechanism for gas phase
128 chemistry (including comprehensive tropospheric and stratospheric chemistry; Emmons et al.,
129 2020) and the four-mode version of the Modal Aerosol Module (MAM4; Liu et al., 2016) for the
130 aerosol scheme. The generation of desert dust particles in MUSICAv0 is calculated based on the
131 Dust Entrainment and Deposition Model (Mahowald et al., 2006; Yoshioka et al., 2017). Dust
132 emissions calculation is sensitive to the model surface wind speed. The dust aerosol processes in
133 the MUSICAv0 simulation are simulated based on the MAM4 model (Liu et al., 2016). MAM4
134 has 4 modes – Aitken, accumulation coarse, and primary carbon modes. Dust is mostly in the
135 accumulation and coarse modes. The MUSICAv0 model source code and the model

136 documentation can be downloaded through
137 <https://wiki.ucar.edu/display/MUSICA/MUSICA+Home> (last access: 3 April 2023).

138 The MUSICAv0 users have the option to create their own model grid. MUSICAv0 is
139 currently being developed and tested for applications over various regions globally
140 (<https://wiki.ucar.edu/display/MUSICA/Available+Grids>), including North America, India, East
141 Asia, South America, Australia, and Korea, among others. (e.g., Schwantes et al., 2022; Tang et
142 al., 2022; Jo et al., 2023). In this study, we develop a model grid for applications in Africa
143 (ne0np4.africa_v5.ne30x4). As shown in Figure 1a, the horizontal resolution is $\sim 111 \text{ km} \times 111 \text{ km}$
144 (i.e., 1° latitude $\times 1^\circ$ equatorial longitude) globally, and $\sim 28 \text{ km} \times 28 \text{ km}$ (i.e., 0.25° latitude \times
145 0.25° equatorial longitude) within the region over Africa. Our simulation uses the default option
146 for vertical layers (i.e., 32 layers from the surface to $\sim 3.64 \text{ hPa}$).

147 Here we run MUSICAv0 with the model grid for Africa for the year 2017, saving 3-hourly
148 output. We use the Copernicus Atmosphere Monitoring Service Global Anthropogenic emissions,
149 (CAMSGLOBANTH) version 5.1 (Soulie et al., 2023) for anthropogenic emissions and the
150 Quick Fire Emissions Dataset (QFED) for fire emissions (Darmanov and da Silva, 2013). CAMS-
151 GLOB-ANTH version 5.1 emissions can be found at <https://eccad3.sedoo.fr/data> (last access: 3
152 April 2023). QFED emissions can be found at
153 <https://portal.nccs.nasa.gov/datashare/ies/aerosol/emissions/QFED/> (last access: 3 April 2023).
154 CAMSGLOBANTH version 5.1 (Soulie et al., 2023) is one of the most widely used global
155 inventories for anthropogenic emissions. CAMSGLOBANTH version 5.1 has been implemented
156 in MUSICAv0, and evaluated in our previous studies (Tang et al., 2022, 2023; Jo et al., 2023).
157 CAMSGLOBANTH version 5.1 does not include information from the Dynamics-Aerosol-
158 Chemistry-Cloud Interactions in West Africa (DACCIWA) project, however, a future version of
159 CAMSGLOBANTH is expected to include DACCIWA for Africa. In future work on this topic,
160 we plan to make use of regional emissions inventories, such as the DACCIWA emission inventory.
161 Plume rise climatology is applied to fire emissions following Tang et al. (2022). In addition, we
162 also include open waste burning (<https://www.acom.ucar.edu/Data/fire/>; Wiedinmyer et al., 2014)
163 emissions in the simulation. The model has the option of a free-running atmosphere or nudging to
164 external meteorological reanalysis. In this simulation, only wind and temperature are nudged to
165 the Modern-Era Retrospective analysis for Research and Applications, Version 2 (MERRA-2;
166 Gelaro et al., 2017) with a relaxation time of 12 hours. MERRA-2 data can be found at
167 <https://disc.gsfc.nasa.gov/datasets?project=MERRA-2> (last access: 3 April 2023).

168 We also added carbon monoxide (CO) tracers in the simulation to understand the source
169 and transport of air pollution. CO tracers in CAM-chem/MUSICAv0 are described in detail by
170 Tang et al. (2019). In this study we include tracers for 6 regions (North Africa, West Africa, East
171 Africa, Central Africa, Southern Africa, and the rest of the world) and 3 emission sources
172 separately (anthropogenic emissions, fire emissions, and open waste burning emissions). In total,
173 there are 18 tagged CO tracers.

174 175 **2.2 WRF-Chem**

176 The Weather Research and Forecasting (WRF) model coupled with Chemistry (WRF-
177 Chem) is a regional chemical transport model. It has been widely used for air quality studies in
178 Africa. In this study we use model results from a WRF-Chem simulation described by Kumar et
179 al. (2022). The WRF-Chem simulation has a grid spacing of 20 km, slightly higher than the
180 MUSICAv0 simulation, and the model domain is highlighted in Figure 1a. The simulation has 36

181 vertical levels from the surface to ~50 hPa. The WRF-Chem simulation uses the Model for Ozone
182 and Related Tracers-4 (MOZART-4) chemical mechanism (Emmons et al., 2010) for tropospheric
183 gas phase chemistry, and the Goddard Global Ozone Chemistry Aerosol Radiation and Transport
184 (GOCART) model (Chin et al., 2002) for aerosol processes. The dust aerosol processes in the
185 WRF-Chem simulation are simulated based on the Goddard Global Ozone Chemistry Aerosol
186 Radiation and Transport (GOCART) model (Chin et al., 2002). Specifically, the dust emission
187 scheme is following the GOCART emission treatment (Ginoux et al., 2001), which is a function
188 of 10-m wind speed, soil moisture, and soil erosion capability. The atmospheric processes of dust
189 are simulated based on the mass mixing ratio and size distribution that has been divided into 5 size
190 bins with effective radii of 0.73, 1.4, 2.4, 4.5 and 8.0 μm . The dust dry and wet depositions are
191 also treated following the GOCART scheme (Chin et al., 2002). The European Centre for Medium
192 Range Weather Forecasts (ECMWF) global reanalysis (ERA-Interim) fields are used for initial
193 and boundary meteorology conditions, while another CAM-chem simulation is used for initial and
194 boundary chemical conditions (Kumar et al., 2022). The WRF-Chem simulation used the global
195 Emission Database for Atmospheric Research developed for Hemispheric Transport of Air
196 Pollution (EDGAR-HTAP v2) for anthropogenic emissions and the Fire Inventory from NCAR
197 version 1.5 (FINNv1.5) (Wiedinmyer et al., 2011) for fire emissions. The WRF-Chem output is
198 saved hourly, however we only use 3-hourly output to match the MUSICAv0 simulation.
199

200 **2.3 ATom**

201 The Atmospheric Tomography mission (ATom; Thompson et al. 2022) was designed to
202 study the impact of human-produced air pollution on greenhouse gases, chemically reactive gases,
203 and aerosols in remote ocean air masses. ATom data (Wofsy et al., 2021) are available at
204 <https://espoarchive.nasa.gov/archive/browse/atom> (last access: 3 April 2023). During the project,
205 the DC-8 aircraft sampled the remote troposphere with continuous vertical profiles. There were
206 four seasonal deployments from the summer of 2016 through the spring of 2018. Here we compare
207 the MUSICAv0 simulation with observations from ATom-2 (January–February 2017) and ATom-
208 3 (September–October 2017). Since the ATom flight tracks were mostly outside the WRF-Chem
209 domain (Figure 1a), we do not compare the WRF-Chem simulation with ATom data. However,
210 we compare chemical species from the MUSICAv0 simulation to the 2-minute merged ATom
211 measurements globally to obtain a benchmark and broader understanding of MUSICAv0
212 performance both within and outside the refined region. The model output is saved along the ATom
213 aircraft flight tracks and with respect to the observational times at run time. Nitric oxide (NO) and
214 ozone (O_3) measurements from the NOAA Nitrogen Oxides and Ozone (NO_yO_3) instrument
215 (Bourgeois et al., 2020, 2021) and the merged CO data (from Quantum Cascade Laser System and
216 NOAA Picarro CO measurements) are used. As we use 2-minute merged ATom measurements,
217 there are 2796 data points in ATom-2 (January–February 2017) and 3369 data points in ATom-3
218 (September–October 2017).
219

220 **2.4 IAGOS**

221 The In-service Aircraft for a Global Observing System (IAGOS) is a European research
222 infrastructure, and was developed for operations on commercial aircraft to monitor atmospheric
223 composition (Petzold et al., 2015). IAGOS data are available at <https://www.iagos.org/iagos-data/>
224 (last access: 3 April 2023). The IAGOS instrument package 1 measures CO, O_3 , air temperature,
225 and water vapor (<https://www.iagos.org/iagos-core-instruments/package1/>). CO is measured by
226 infrared absorption using the gas filter correlation technique (Precision: $\pm 5\%$, Accuracy: ± 5 ppb)

227 while O₃ is measured by UV absorption at 253.7 nm (Precision: ±2%, Accuracy: ±2 ppb). We use
228 airborne measurements of CO, O₃, air temperature, and water vapor from IAGOS for model
229 evaluation. The locations of the IAGOS flight tracks over Africa are shown in Figure 1b. The
230 model results and IAGOS data comparisons are conducted separately for five African sub-regions
231 (defined in Figure 1b). The IAGOS instruments are onboard commercial airliners and the sampling
232 may not be representative of the whole sub-regions. For example, IAGOS data over southern
233 Africa only covers the west part of southern Africa.

234

235 **2.5 Ozonesondes**

236 The ozonesonde is a balloon-borne instrument that measures atmospheric O₃ profiles
237 through the electrochemical concentration cell using iodine/iodide electrode reactions (Thompson
238 et al., 2017), with records of temperature, pressure, and relative humidity from standard
239 radiosondes. NASA/GSFC SHADOZ data are available at <https://tropo.gsfc.nasa.gov/shadoz/> (last
240 access: 3 April 2023). We use ozonesonde data from Southern Hemisphere ADDitional
241 OZonesondes (NASA/GSFC SHADOZ; Thompson et al., 2017; Witte et al., 2017, 2018).
242 Specifically, ozonesonde data from four sites are used (Figure 1b): Ascension (Ascension Island,
243 U.K.), Nairobi (Kenya), Irene (South Africa), and La Reunion (La Réunion Island, France). The
244 average O₃ measurement uncertainty ranged from 5–9% for the ozonsonde data used in this study.

245

246 **2.6 WDCGG**

247 Monthly surface CO measurements from the World Data Center for Greenhouse Gases
248 (WDCGG; operated by the Japan Meteorological Agency in collaboration with the World
249 Meteorological Organization) are used for model evaluation. WDCGG data are available at
250 <https://gaw.kishou.go.jp/> (last access: 3 April 2023). Data from six sites are used (Figure 1b),
251 namely (Ascension Island, U.K.), Assekrem (Algeria; remote site located in Saharan desert),
252 Gobabeb (Namibia; located at the base of a linear sand dune, next to an interdune plain), Cape
253 Point (South Africa; site exposed to the sea on top of a cliff 230 meters above sea level), Izana
254 (Tenerife, Spain; located on the Island that is ~300 km west of the African coast), and Mare
255 (Seychelles; near an international airport).

256

257 **2.7 Surface PM_{2.5}**

258 At the U.S. embassies, regulatory-grade monitoring data are collected with Beta
259 Attenuation Monitors (BAMs), using a federal equivalent monitoring method, with an accuracy
260 within 10% of federal reference methods (Watson et al., 1998; U.S. EPA, 2016). These instruments
261 are operated by the U.S. State Department and the U.S. EPA, and data are available through
262 AirNow (<https://www.airnow.gov/international/us-embassies-and-consulates/>). We use the
263 measurements at the U.S. embassy locations in Addis Ababa Central (Ethiopia, 9.06° N, 38.76° E)
264 and Kampala (Uganda, 0.30° N, 32.59° E) for the year 2017 as references (Malings et al., 2020)
265 to match our simulations. The raw data are made available hourly and for this study we use daily
266 mean PM_{2.5} for comparison with model simulations. Djossou et al. (2018) presented PM_{2.5}
267 measurements from Feb 2015 to March 2017 at two cities in West Africa – Abidjan and Cotonou
268 (Figure 1b). In Abidjan, there were three sites that are representative of traffic, waste burning at
269 landfill, and domestic fires. The site in Cotonou is close to traffic emissions. The concentrations
270 of PM_{2.5} particles were measured at a weekly time step by the ambient air pumping technique
271 (Djossou et al., 2018). We compare model results with the weekly PM_{2.5} measurements from the
272 sites in Abidjan and Cotonou for January–March 2017.

273
274
275
276
277
278
279
280
281
282
283
284
285
286
287
288
289
290
291
292
293
294
295
296
297
298
299
300
301
302
303
304
305
306
307
308
309
310
311
312
313
314
315
316
317
318

2.8 MOPITT

The Measurements of Pollution in the Troposphere (MOPITT) instrument on board the NASA Terra satellite provides both thermal-infrared (TIR) and near-infrared (NIR) radiance measurements since March 2000. MOPITT CO data can be accessed through <https://search.earthdata.nasa.gov/search> (last access: 3 April 2023). Retrievals of CO column density and vertical profiles are provided in a multispectral TIR–NIR joint product which has sensitivity to near-surface as well as free tropospheric CO (Deeter et al., 2011; Worden et al., 2010). Here we use the MOPITT Version 9 Level 2 CO column product (Deeter et al., 2022) over Africa to evaluate the MUSICAv0 and WRF-Chem simulations. MOPITT Version 9 has significant updates to the cloud detection algorithm and NIR calibration scheme. The MOPITT satellite pixel size is $\sim 22 \text{ km} \times 22 \text{ km}$, and the overpass time is $\sim 10:30$ am local time in 2017. When comparing model outputs to MOPITT the recommended data quality filter is applied and model outputs are interpolated to the MOPITT retrievals in space and time. To perform quantitative comparisons, the MOPITT averaging kernel and a priori are used to transform the model CO profiles to derive model column amounts.

2.9 OMI NO₂ (QA4ECV)

Tropospheric column NO₂ from the Ozone Monitoring Instrument (OMI) on board Aura is compared to the model in this study. Specifically, the NO₂ product from the quality assurance for the essential climate variables (QA4ECV) project is used (Boersma et al., 2017a; Compernolle et al., 2020). OMI NO₂ data are available at <https://www.temis.nl/qa4ecv/no2.html> (last access: 3 April 2023). The satellite pixel size is $\sim 13 \text{ km} \times 25 \text{ km}$, and the overpass time is $\sim 1:40$ pm local time in 2017. A data quality filter was applied following the Product Specification Document (Boersma et al., 2017b; `processing_error_flag = 0`, `solar_zenith_angle < 80`, `snow_ice_flag < 10` or `snow_ice_flag = 255`, `amf_trop/amf_geo > 0.2`, and `cloud_radiance_fraction_no20 <= 0.5`). Model profiles were transformed using the provided tropospheric air mass factor (AMF) and averaging kernels.

2.10 OMI HCHO (QA4ECV)

We also use tropospheric column HCHO from OMI in this study. Similar to OMI NO₂, we also use OMI HCHO product from QA4ECV (De Smedt et al., 2017a). OMI HCHO data are available at <https://www.temis.nl/qa4ecv/hcho.html> (last access: 3 April 2023). A data quality filter was applied following the Product User Guide (De Smedt et al., 2017b; `processing_error_flag = 0` and `processing_quality_flag = 0`). Model profiles were transformed using provided averaging kernels. We note that HCHO retrievals are subject to relatively large uncertainties compared to other satellite products used in this study. Therefore, the comparisons between model results and the OMI HCHO product only indicate the model-satellite discrepancies rather than determining model deficiencies. In addition, the WRF-Chem simulation from Kumar et al. (2022) does not include HCHO in the output and hence will not be compared.

2.11 MODIS AOD

The aerosol optical depth (AOD) product (550 nm) from the Moderate Resolution Imaging Spectroradiometer (MODIS) on board Terra NASA Terra satellite is used. MODIS AOD data can be accessed through <https://search.earthdata.nasa.gov/search> (last access: 3 April 2023). Specifically, we used the MODIS Level 2 Collection 6.1 product (MOD04_L2; Levy et al., 2017).

319 Deep Blue Aerosol retrievals are used (Hsu et al., 2013; Levy et al., 2013) to include retrievals
320 over the desert. The MODIS satellite pixel size is $\sim 1 \text{ km} \times 1 \text{ km}$, and the overpass time is $\sim 10:30$
321 am local time. East and Southern Africa have complex terrain due to mountains and rift valleys.
322 This may lead to some uncertainties in MODIS AOD retrievals.

323

324 **2.12 AERONET AOD**

325 We use AOD measurements from the AErosol RObotic NETwork (AERONET; Holben et
326 al., 1998, 2001). AERONET data can be accessed through <https://aeronet.gsfc.nasa.gov/>. We use
327 Level 2 daily data (quality assured), with pre-field and post-field calibration applied and has been
328 automatically cloud cleared and manually inspected. AOD at 675 nm from AERONET data are
329 converted to AOD at 550 nm using provided Angstrom exponent to compare with modeled AOD
330 at 550 nm.

331

332 **2.13 SAAQIS**

333 We also compare model results with $\text{PM}_{2.5}$, CO, NO_2 , and O_3 measurements from South
334 Africa Air Quality Information System (SAAQIS; Gwaze et al., 2018; Tshela et al., 2019).
335 SAAQIS is available at <http://saaqis.environment.gov.za/>. The data are hourly and we calculate
336 daily average values before compare with model results. Similar to Zhang et al. (2021), we
337 removed negative values and only calculate daily averages when 75% or more of the hourly data
338 are available.

339

340 **3. Model comparisons with satellite data and evaluation with in situ observations**

341 Africa includes a wide range of environments and emissions source. Therefore, in this
342 section we separate the continent in five sub-regions for analysis following Kumar et al. (2022).
343 CO is a good tracer of anthropogenic and biomass burning emissions and modeled CO tracers are
344 used in this section to understand sources. CO is a commonly used tracer in models with only one
345 photochemical sink and an intermediate lifetime (e.g., Tang et al., 2019). CO tracers also allow
346 clear identification of simulated anthropogenic and biomass burning contributions. Therefore,
347 tagging CO is computationally efficient and tagged CO is relatively reliable as a tracer in models.
348 Meteorology has a significant impact on the distributions of pollutants across the regions (e.g.,
349 Gordon et al., 2023). The CO tracers in the model go through the same model processes (e.g.,
350 transport) as CO. Therefore, the source contribution shown by the CO tracers is a result of both
351 emissions and transport. Figure 2 shows the seasonal averages of CO column distributions over
352 Africa from MOPITT along with the MUSICAv0 and WRF-Chem biases. The highest levels of
353 CO in these maps are primarily associated with biomass burning, which moves around the
354 continent with season. Both MUSICAv0 and WRF-Chem simulations underestimate the CO
355 column compared to MOPITT (Figures 3a and 3b). Overall, MUSICAv0 agrees better with the
356 OMI tropospheric NO_2 column (Figure 3c) and MODIS AOD (Figure 3e) than WRF-Chem
357 (Figures 3d and 3f). The MUSICAv0 simulation overall has lower tropospheric HCHO column
358 than OMI in all regions and seasons (Figure 3g). Spatial distributions of model biases against the
359 OMI tropospheric NO_2 column, MODIS AOD, and OMI tropospheric HCHO column are included
360 in Figures 4 and Figures S1–S2. In this section we compare the model results with satellite data
361 and in situ observations over sub-regions in Africa and oceans near Africa (Figure 1b). AERONET
362 data are overlaid with MODIS data in Figure 4. Overall, MODIS and AERONET AOD are
363 consistent.

364

365 3.1 North Africa

366 Over North Africa, both MUSICAv0 and WRF-Chem simulations underestimate the CO
367 column during 2017 (Figures 2 and 3). As shown by the tagged model CO tracers (Figure 5), CO
368 over North Africa is mainly driven by transport of CO from outside the continent and
369 anthropogenic emissions. The model underestimation compared to the MOPITT CO column is
370 consistent with the results of the comparisons with surface CO observations from WDCGG at the
371 two sites located in North Africa (Assekrem and Izana; Figures 6a and 6c). At the two surface
372 sites, the composition of source types and source regions are close to the composition of source
373 types and source regions of the column average over North Africa (Figure 5 and Figures S3 and
374 S4), hence the two sites are representative of the background conditions of North Africa.
375 Compared to MODIS AOD, WRF-Chem has a mean bias of 0.36 whereas MUSICAv0's mean
376 bias is 0.17 for 2017. The model AOD biases over North Africa are likely driven by dust. No
377 comparison is made with IAGOS O₃ in North Africa due to data availability.

378

379 3.2 West Africa

380 Over West Africa, fire and anthropogenic emissions are both important for CO pollutant
381 and fire impacts peak in DJF (December, January, and February). Compared to the MOPITT CO
382 column, the mean bias of MUSICAv0 and WRF-Chem for West Africa peak around February –
383 the dry season of the Northern Hemisphere (Figure 3). In February, the MUSICAv0 mean bias is
384 -1.1×10^{18} molecules/cm² and WRF-Chem mean bias is -7.5×10^{17} molecules/cm², which are likely
385 driven by fire emission sources (Figure 5). Model comparisons with IAGOS CO also show a
386 similar bias – both model simulations underestimate CO at all vertical levels. The underestimation
387 peaks during DJF and below 600 hPa (Figure 7). As for MODIS AOD, WRF-Chem has the mean
388 bias 0.69 whereas MUSICAv0's mean bias is 0.15, respectively. Similar to North Africa, the model
389 biases in AOD over West Africa are also likely driven by dust and biomass burning. We also
390 compare modeled O₃ with IAGOS O₃ observations (Figure 8).

391 Over West Africa, both models agree well with the IAGOS O₃ observations below 800 hPa
392 (mean bias ranges from -1 to -4 ppb). Above 800 hPa over West Africa, WRF-Chem
393 underestimates O₃ while MUSICAv0 overestimates O₃. Overall, MUSICAv0 consistently
394 overestimates O₃ above 800 hPa in all seasons while the direction of WRF-Chem bias changes
395 with seasons (Figure 8). When MUSICAv0 overestimates O₃, the bias is in general larger at the
396 higher altitude of the troposphere. The concentration of the model stratospheric ozone tracer, O₃S,
397 is also larger at the higher altitude in DJF (Figure 10). The correlation of modeled O₃ and O₃S is
398 0.54, and the correlations of O₃S and model O₃ bias (modeled O₃ minus IAGOS O₃) is 0.35 over
399 West Africa, implying the overestimation of O₃ in the upper troposphere could be partially driven
400 by too strong stratosphere-to-troposphere flux of ozone. Previous studies also found impacts of
401 stratosphere-to-troposphere flux of ozone over West Africa (e.g., Oluleye et al., 2013). Lightning
402 NO emissions can also impact O₃ in the upper troposphere. The MUSICAv0 simulation has
403 somewhat (~3 times) higher lightning NO emissions (Figure S5) compared to a standard CAM-
404 chem simulation (not shown), therefore the high ozone in the upper troposphere may be due to an
405 over-estimate of lightning NO. We also compared our modeled lightning NO emissions with a
406 multi-year average climatology (2008-2015) from Maseko et al. (2021) over South Africa, and
407 found that the seasonal cycle from MUSICAv0 and standard CAM-chem are consistent with the
408 climatology. The magnitude of MUSICAv0 lightning NO emissions overall agree better with the
409 climatology compared to that from standard CAM-chem simulation. Impacts of lightning NO
410 emissions on upper troposphere O₃ in MUSICAv0 will be investigated and evaluated further in the

411 future. A brief comparison with IAGOS measurements of air temperature and water vapor profiles
412 over West Africa as well as other sub-regions shows that MUSICAv0 overall agrees well with
413 these meteorological variables (Figure S6).

414 We compare the models with weekly PM_{2.5} measurements at 3 sites in Abidjan
415 (representing domestic fires emissions, waste burning at landfill, and traffic) and 1 site in Cotonou
416 representing traffic emissions (Figure S7). Overall, both models underestimate PM_{2.5} at the three
417 Abidjan sites, especially near the domestic fire emissions where measured PM_{2.5} exceeded 400
418 µg/m³. We include open burning emissions in the MUSICAv0 simulation however the significant
419 underestimation point to the possibility of missing emissions. Moreover, these three sites in
420 Abidjan are within the same city and near strong emission sources and hence are challenging for
421 both models to resolve. In fact, they fall into the same model grids and therefore model values at
422 the three sites are the same for both models. This demonstrates the need of higher model resolution
423 to resolve variabilities of air quality in a city.

424

425 **3.3 Central Africa**

426 Compared to MOPITT CO column, the mean bias of MUSICAv0 and WRF-Chem for
427 Central Africa varies with seasons (Figure 3) but peaks during the dry season in September
428 (MUSICAv0 mean bias of -1.0×10^{18} molecules/cm²; WRF-Chem mean bias of -1.2×10^{18}
429 molecules/cm²). The tagged model CO tracers show that in September, local fire emissions are the
430 dominant driver of CO in Central Africa (Figure 5). Compared to the IAGOS CO profiles (Figure
431 7), both models have the largest bias over Central Africa among the sub-regions in Africa – mean
432 bias of MUSICAv0 and WRF-Chem are -46 ppb and -36 ppb, respectively. The high bias over
433 Central Africa mainly occurs during the fire season. In central Africa, both models also
434 underestimate NO₂ (mean biases of MUSICAv0 and WRF-Chem are -1.5×10^{14} and -5.5×10^{14}
435 molecules/cm², respectively). The underestimations in both CO and NO₂ by the two model
436 simulations are likely driven by the underestimation in fire emissions. Indeed, the emission
437 estimates from the newest version of FINN (FINNv2.5; Wiedinmyer et al., 2023) are higher
438 compared to both QFED (used in the MUSICAv0 simulation) and FINNv1.5 (used in the WRF-
439 Chem simulation) in this region.

440 Model mean bias of HCHO (-1.3×10^{16} molecules/cm² for the whole 2017) over Central
441 Africa is the largest among the five regions (Figure 3). The spatial distribution of HCHO bias
442 (Figure S2) largely co-locates with the vegetation (Figure 9). Over the barren or sparsely vegetated
443 area in North Africa, HCHO biases are relatively small while over the vegetated area HCHO bias
444 are relatively large. Over North Africa, the mean bias is -0.66×10^{16} molecules/cm² for the whole
445 2017 whereas over the other four regions, the mean bias ranges from -0.93×10^{16} molecules/cm² to
446 -1.31×10^{16} molecules/cm² for the whole 2017. This indicates that the negative bias in MUSICAv0
447 HCHO could be due to underestimated biogenic emissions in the model. In addition, the
448 underestimation of HCHO in Central Africa (Figure S2) co-locates with the underestimation of
449 CO in time and space (Figure S1), implying that fire emissions that contributed to model CO biases
450 may also contribute to the HCHO underestimation in MUSICAv0 during fire season. It is
451 important to note that the uncertainty of OMI tropospheric HCHO column is relatively large
452 compared to other satellite products. Here the averaged retrieval uncertainty (random and
453 systematic) is ~120%.

454 When compared to the IAGOS O₃ profiles over Central Africa (Figure 8), both models
455 agree well with the IAGOS O₃ observations below 800 hPa (mean bias ranges from -1 to -4 ppb).
456 Above 800 hPa, WRF-Chem underestimates O₃ while MUSICAv0 overestimates O₃. The

457 correlation of modeled O₃ and O₃S is 0.67, and the correlations of O₃S and model O₃ bias is 0.50
458 over Central Africa, indicating O₃ overestimation in Central Africa are more likely to be impacted
459 by stratosphere-to-troposphere flux of ozone than that in West Africa.

460

461 **3.4 East Africa**

462 CO over East Africa is dominated by local emissions and inflow from outside the continent.
463 Fire and anthropogenic emissions contribute approximately the same to CO over East Africa
464 (Figure 5). Both MUSICAv0 and WRF-Chem simulations underestimate the CO column
465 compared to MOPITT (Figure 3), and the WRF-Chem simulation also underestimate the
466 tropospheric NO₂ column compared to OMI. The biases in CO column and tropospheric NO₂
467 column peak in September. One possible driver could be fire emissions from other regions (Figure
468 5), however, further studies will be needed to address this.

469 Compared to IAGOS O₃ profiles over East Africa, biases of MUSICAv0 below 600 hPa
470 has a seasonal variation while over 600 hPa are consistently positive (Figure 8). The correlations
471 of O₃S and model O₃ bias against IAGOS data is 0.50 in the region. The correlations between O₃S
472 and model O₃ bias are highest over Central and East Africa compared to other regions, indicating
473 stratosphere influence are strongest in these two regions among the sub-regions. Central and East
474 Africa are relatively more mountainous therefore topography driven stratospheric intrusions might
475 be expected. The Nairobi ozonesonde site is located in East Africa (Figure 1b). When comparing
476 to the O₃ profiles from ozonesondes (Figure 10), MUSICAv0 overall overestimates O₃ in the
477 troposphere at the four sites while WRF-Chem tends to underestimate O₃ in the free troposphere
478 (below 200 hPa). The Nairobi site is an exception where both MUSICAv0 and WRF-Chem
479 simulations significantly overestimate O₃ in all seasons (mean bias of MUSICAv0 and WRF-
480 Chem below 200 hPa are 27 ppb and 20 ppb, respectively). Among the four ozonesonde sites,
481 correlations of model bias of O₃ and O₃S are highest at the Nairobi site (0.74) where the model
482 significantly overestimates O₃. The results of model-ozonesonde comparisons are consistent with
483 the results of model-IAGOS comparisons and indicate a potential issue in modeled stratosphere-
484 to-troposphere flux of ozone.

485 We compare the model results with PM_{2.5} measurements from two surface sites in East
486 Africa (Addis Ababa and Kampala; Figure 1b). Despite using different aerosol methods and
487 emission inventories, both MUSICAv0 and WRF-Chem underestimate surface PM_{2.5} when
488 compared to observations at the two sites (Figure 11). The errors in PM_{2.5} concentrations at the
489 U.S. Embassy in Kampala are especially prominent. However, both models approximate the
490 variation of the PM_{2.5} in both locations. Many factors contribute to the inconsistency in the
491 magnitude of modeled PM_{2.5} concentrations. For instance, emission inventories in this region
492 require additional improvement. In Uganda, increasing motor vehicle ownership and burning
493 biomass for domestic energy use contribute to ambient PM_{2.5} levels (Clarke et al., 2022; Petkova
494 et al., 2013; Kinney et al., 2011). Detailed PM_{2.5} composition measurements would also help to
495 pinpoint the cause of inaccuracies (Kalisa et al., 2018). Model resolutions could also be a potential
496 reason for the underestimation. Over Kampala, high spatial variability of PM_{2.5} over the urban
497 environment can contribute to model bias (Atuhaire et al., 2022), as also shown by the AirQo low-
498 cost air quality monitors (Sserunjogi et al., 2022; Okure et al., 2022).

499

500 **3.5 Southern Africa**

501 Among the five regions, MUSICAv0 has the lowest mean bias in CO (-3.2×10^{17}
502 molecules/cm² annually) over Southern Africa (Figure 3). WRF-Chem also has low mean bias and

503 RMSE in CO over Southern Africa except for the months of September, October, and November
504 (SON) period where WRF-Chem has larger CO mean bias (-6.2×10^{17} molecules/cm²) than
505 MUSICAv0. Tagged model CO tracers indicate that CO over Southern Africa is significantly
506 impacted by CO emissions from Central Africa, East Africa, Southern Africa, and inflow from
507 outside the continent. As for the source types, anthropogenic and fire emissions are both important
508 and fire impacts peak in September (e.g., Archibald et al., 2009, 2010; Archibald 2016). There are
509 two WDCGG sites located in Southern Africa (Figure 1b; Gobabeb and Cape Point). When
510 compared to surface CO observations from WDCGG, both models consistently underestimate CO
511 by up to 40% at most sites. The Cape Point site in Southern Africa is an exception (Figure 6) where
512 MUSICAv0 overestimates CO by 40 ppb (annual mean; and up to 78 ppb in May 2017). CO tracers
513 in the model (Figures S3 and S4) show that the simulated CO at Cape Point is mainly driven by
514 anthropogenic CO emissions from Southern Africa. Therefore, the overestimation of CO at Cape
515 Point by MUSICAv0 may be due to an overestimation of emissions in South Africa. Note that the
516 Cape Point measurement site is located on the tip of southern Africa and has a strong impact from
517 clean marine air (Labuschagne et al., 2018), which the model likely cannot represent accurately.

518 As for NO₂, WRF-Chem underestimates tropospheric NO₂ column in most regions except
519 for Southern Africa (Figure 3). Over Southern Africa, WRF-Chem overestimates NO₂ especially
520 during June, July, and August (JJA). MUSICAv0 also tends to overestimates NO₂ at the same
521 location in JJA however the bias is not as large as for WRF-Chem.

522 MUSICAv0 simulation overall has a lower mean bias (0.14 annually) than the WRF-Chem
523 simulation (mean bias of 0.31 annually) compared to MODIS AOD with Southern Africa being
524 the only exception (Figure 3). Over Southern Africa, MUSICAv0 overestimates AOD by ~0.21
525 annually (Figure 3) and the bias peaks in January (mean bias=0.45). This overestimation in AOD
526 over Southern Africa is not seen in WRF-Chem. It is likely that the MUSICAv0 overestimation in
527 AOD over Southern Africa is also due to biases in modeled dust as the AOD bias is co-located
528 with the only barren or sparsely vegetated area in Southern Africa (Figure 9 and Figure S2).

529 Over Southern Africa, MUSICAv0 tends to overestimate O₃ compared to IAGOS at all
530 levels at all seasons in 2017 (Figure 8). The MUSICAv0 O₃ bias is 5-10 ppb below 800 hPa for
531 the four seasons and 23-39 ppb at 225 hPa. The concentration of O₃S over Southern Africa is
532 higher than those over other regions. However, the correlation of O₃S and model O₃ bias is lower
533 than other regions (0.13) indicating stratosphere-to-troposphere flux of ozone may not be the main
534 driver of O₃ bias over Southern Africa even though stratosphere-to-troposphere flux of ozone are
535 relatively strong in the region (e.g., Leclair De Bellevue et al., 2006; Clain et al., 2009; Mkololo
536 et al., 2020). The Irene ozonesonde site is located in Southern Africa (Figure 1b). Compared to the
537 ozonesonde O₃ profiles at the Irene site, however, the sign of MUSICAv0 has a seasonal variation
538 (Figure 10e-10h). For example, at 675–725 hPa, MUSICAv0 O₃ bias in MAM and JJA is 3-9 ppb
539 whereas in SON and DJF it is -2 to -6 ppb. The IAGOS measurements and the Irene ozonesonde
540 site are not co-located, so the difference is expected due to the different sampling locations and
541 environment. Compared to other ozonesonde sites, the correlation of O₃S and model O₃ bias over
542 Southern Africa is lower (0.14) and MUSICAv0 agrees relatively well with observations, which
543 is consistent with the comparison results with IAGOS data (Figure 8).

544 We further compare MUSICAv0 and WRF-Chem results with surface PM_{2.5}, CO, NO₂,
545 and O₃ measurements from SAAQIS in South Africa (Figures S8-S11). Overall, the performance
546 of MUSICAv0 and WRF-Chem compared to SAAQIS data are similar. Both models underestimate
547 surface CO in most sites (consistent with the comparisons with satellites) with exceptions near
548 Gauteng (industrialized and urbanized region). Compared to SAAQIS sites near Cape Point,

549 MUSICAv0 does not show overestimation which is opposite to the overestimation compared to
550 WDCGG Cape Point site. The maximum value of monthly CO observations from WDCGG Cape
551 Point site in 2017 is ~150 ppb whereas the seasonal mean values of SAAQIS CO measurements
552 near Cape Point site can be up to 600 ppb. SAAQIS CO measurements near Cape Point shows
553 relatively large spatial variability, indicating (1) that there may be a wide range of emission sources
554 that are poorly captured by the model and (2) a large role of local sources and potentially complex
555 meteorology. In addition, uncertainties in observations could also contribute to the difference. Both
556 models tend to overestimate NO₂ near Gauteng, which may be related to local emissions. Both
557 models can either overestimate or underestimate PM_{2.5} and/or O₃ at different SAAQIS sites. The
558 model bias in PM_{2.5} and O₃ shows large spatial variability especially near Gauteng. Higher model
559 resolution is needed to address the highly complex and diverse environment in the region. Lastly,
560 it is worth pointing out that in South Africa, both models have evident bias in PM_{2.5} near Gauteng
561 (Figure S11) however modeled AOD from both models agree relatively well with MODIS and
562 AERONET (Figure 4). More studies are needed to understand this feature.

563

564 **3.6 Oceans near Africa**

565 We compare the CO, NO, and O₃ from the MUSICAv0 simulation with measurements
566 from ATom-2 and ATom-3 in 2017 (Figure 1a) to provide a global benchmark. Measurements
567 made over the Atlantic Ocean and Pacific Ocean, and in January-February (Jan-Feb) and
568 September-October (Sep-Oct) are compared separately (Figures 11 and 12). The comparison was
569 made with data averaged into 10° latitude and 200 hPa bins. Overall, the model consistently
570 underestimates CO globally in both seasons. The underestimation of CO is a common issue in
571 atmospheric chemistry models and could be due to various reasons, including emissions,
572 deposition, and chemistry (e.g., Fisher et al., 2017; Shindell et al., 2006; Stein et al., 2014; Tilmes
573 et al., 2015; Tang et al., 2018; Gaubert et al., 2020). Specifically for our MUSICAv0 simulation
574 in this study, the model bias in CO is relatively large (up to 52 ppb) over the Northern Hemisphere
575 (especially at high latitude and near the surface) and small over the Southern Hemisphere (Figures
576 11 and 12). Over the Atlantic Ocean, the bias in CO is larger in September-October than Jan-Feb
577 in both the Northern Hemisphere (-30 ppb in Jan-Feb versus -34 ppb in Sep-Oct) and Southern
578 Hemisphere (-11 ppb in Jan-Feb versus -14 ppb in Sep-Oct). Over the Pacific Ocean, however, the
579 CO bias is similar for both time periods in the Northern Hemisphere (-30 ppb) while in the
580 Southern Hemisphere, the CO bias changes significantly from -8 ppb in Jan-Feb to -16 ppb in Sep-
581 Oct. The changes in CO bias over the Southern Hemisphere are likely due to seasonal change in
582 fire emissions. Overall, the mean biases (Figures 11 and 12) suggest that the simulation agrees
583 better with ATom observations in the Southern Hemisphere than in the Northern Hemisphere, and
584 in Jan-Feb than in Sep-Oct (Figures 11 and 12), consistent with Gaubert et al. (2016).

585 In both seasons and both hemispheres, the model in general overestimates O₃ in the
586 stratosphere/UTLS (upper troposphere and lower stratosphere) by up to 38 ppb (above 200 hPa).
587 In the troposphere (below 200 hPa), the model overall agrees well with the ATom data over the
588 Pacific Ocean in the Southern Hemisphere (in most cases the bias is less than ±5 ppb). However,
589 over the Atlantic Ocean in the Southern Hemisphere, MUSICAv0 tends to overestimate O₃,
590 especially in Jan-Feb. In the troposphere of the Northern Hemisphere, MUSICAv0 consistently
591 overestimates O₃ over both oceans and both seasons. The positive bias in O₃ decreases from the
592 upper troposphere towards the surface, indicating that the overestimation of O₃ in the troposphere
593 may be due to stratosphere-to-troposphere flux of ozone. This was also noted for other global
594 models (Bourgeois et al. 2021). Thompson et al. (2014) found O₃ at the Irene site is also influenced

595 by long-range transport of growing pollution in the Southern Hemisphere, which could also
596 contribute to the model bias. As for NO, the model tends to overestimate NO above 200 hPa
597 (approximately the stratosphere and Upper Troposphere-Lower Stratosphere; UTLS) by up to 50
598 ppt. Overall, the NO biases can be either positive or negative depending on location and season.
599 The distributions of NO bias (Figures 11 and 12) do not show an overall spatial pattern, unlike
600 those for CO (which changes monotonically with latitude) or O₃ (which changes monotonically
601 with altitude).
602

603 **4. Model application: identifying key regions in Africa for future in situ observations and** 604 **field campaign(s)**

605 As a demonstration of the application of MUSICA_{v0}, here we use the results of model-
606 satellite comparisons to identify potential regions where the atmospheric chemistry models need
607 to be improved substantially. More field campaigns and more in situ observations would not only
608 provide observational benchmark dataset to understand and improve the modeling capability in
609 the region, but would be also useful for the validation and calibration of satellite products. Here
610 we use Taylor score to quantify model-satellite discrepancies. Taylor score (Taylor, 2001) is
611 defined by

$$612 \quad S = \frac{4(1+R)}{(\hat{\sigma}_f+1/\hat{\sigma}_f)^2(1+R_0)}$$

613 where $\hat{\sigma}_f$ is the ratio of σ_f (standard deviation of the model) and σ_r (standard deviation of
614 observations), R is correlation between model and observations, and R_0 is the maximum
615 potentially realizable correlation (=1 in this study). Taylor score ranges from 0 to 1 and a higher
616 Taylor score indicates better satellite-model agreement. To identify potential locations, we
617 separate the Africa continent into 5° × 5° (latitude × longitude) pixels as shown in Figure 14. And
618 for each pixel, we calculate Taylor scores of MUSICA_{v0} compared to the three satellite Level 2
619 products (e.g., MOPITT CO column retrievals, OMI tropospheric NO₂ column retrievals, and
620 MODIS AOD) separately. Then three Taylor scores are summed up to obtain the total Taylor score
621 for MUSICA_{v0} (ranges from 0 to 3) as shown in Figures 13a-13e. A similar calculation is
622 conducted for WRF-Chem (Figures 13f-13j). Note that we did not include Taylor scores for HCHO
623 in the total Taylor score due to that (1) WRF-Chem simulations did not save HCHO output, and
624 (2) the HCHO retrievals have relatively high uncertainties (Taylor scores of MUSICA_{v0} compared
625 to OMI tropospheric HCHO column retrievals are provided separately in Figure S12).

626 Overall, both MUSICA_{v0} and WRF-Chem have low total Taylor scores in the 30°E – 45°E,
627 5°S – 5°N region in East Africa (a region of 15° longitude × 10° latitude) during MAM (March,
628 April, and May), JJA (June, July, and August), and SON (September, October, and November), as
629 highlighted in Figure 14, indicating relatively large model-satellite discrepancies in the region.
630 Besides the 30°E – 45°E, 5°S – 5°N region highlighted in Figure 14, there are a few other regions
631 with low Taylor scores for both MUSICA_{v0} and WRF-Chem such as 10°E – 20°E, -30°S – -20°N
632 region and the east of Madagascar.

633 The 30°E – 45°E, 5°S – 5°N region (a sub-region in East Africa) is also the region where
634 the Nairobi ozonesonde site and the Kampala surface PM_{2.5} site are located (Figure 1b). As
635 discussed above, both MUSICA_{v0} and WRF-Chem significantly overestimate O₃ (Figure 10) and
636 largely underestimate PM_{2.5} (Figure 11) in the region. More in situ observations or future field
637 campaigns in the region can substantially help in the understanding model-satellite and model-in
638 situ observation discrepancies and improving model performance.

639 The 30°E – 45°E, 5°S – 5°N region (a sub-region in East Africa) is potentially a favorable
640 location for future field campaign(s) not only because of the large model-satellite and model-in
641 situ observation discrepancies, but also due to that the population density is high and landcover
642 are diverse in the region (Figure 9). The relatively high population density in the region indicates
643 that improved air quality modeling in the region can benefit a large population. A diverse landcover
644 indicates more processes/environments can be sampled. CO tracers in the model (Figure 15) show
645 that CO over the region is mainly driven by both anthropogenic and fire emissions. Anthropogenic
646 emissions play a more important role in the 30°E – 45°E, 5°S – 5°N region compared to East
647 Africa in general (Figures 4 and 14). In terms of source regions, emissions from East Africa and
648 inflow from outside the continent are the dominant source, with some contributions from Central
649 Africa. Note that the source analyses using model tracers may be subject to uncertainties in the
650 emission inventories, in this case CAMSv5.1, QFED, and the waste burning inventory used here.
651 As discussed above (e.g., Section 3.4), there might be missing sources in the region. In addition,
652 emission factors used in many emission inventories are based on measurements outside the
653 continent of Africa (e.g., Lamarque et al. 2010; Klimont et al., 2013; Pokhrel et al. 2021). It is not
654 clear so far if these emission factors are applicable to emissions in Africa (e.g., Keita et al., 2018).
655 Therefore, a field campaign in the region can help address these issues.

656 We would like to point out that in this analysis, the key area is selected using 3 satellite
657 products/chemical species and two models. The Taylor score is a comprehensive measure of model
658 performance that accounts for variance and correlation, however, other models and types of
659 comparisons may provide different answers.

660

661 **5. Conclusions**

662 Africa is one of the most rapidly changing regions in the world and air pollution is a
663 growing issue at multiple scales over the continent. MUSICAv0 is a new community modeling
664 infrastructure that enables the study of atmospheric composition and chemistry across all relevant
665 scales. We developed a MUSICAv0 grid with Africa refinement (~28 km × 28 km over Africa and
666 ~110 km × 110 km for the rest of the world) and conducted the simulation for the year 2017. We
667 evaluated the model with in situ observations including ATom-2 and ATom-3 airborne
668 measurements of CO, NO, and O₃, IAGOS airborne measurements of CO and O₃, O₃ profiles from
669 ozonesondes, surface CO observations from WDGCC, and surface PM_{2.5} observations from two
670 U.S. Embassy locations. We then compare MUSICAv0 with satellite products over Africa, namely
671 MOPITT CO column, MODIS AOD, OMI tropospheric NO₂ column, and OMI tropospheric
672 HCHO column. Results from a WRF-Chem simulation were also included in the evaluations and
673 comparisons as a reference. Lastly, as an application of the model, we identified potential African
674 regions for in situ observations and field campaign(s) based on model-satellite discrepancies
675 (quantified by Taylor score), with regard to model-in situ observation discrepancies, source
676 analyses, population, and land cover. The main conclusions are as follows.

677 (1) When comparing to ATom-2 and ATom-3, MUSICAv0 consistently underestimates
678 CO globally. Overall, the negative model bias increases with latitude from the Southern
679 Hemisphere to the Northern Hemisphere. MUSICAv0 also tends to overestimate O₃ in the
680 stratosphere/UTLS, and the positive model bias overall decreases with altitude.

681 (2) The MUSICAv0 biases in O₃ when compared to ATom, IAGOS, and ozonesondes are
682 likely driven by stratosphere-to-troposphere fluxes of O₃ and lightning NO emissions.

683 (3) Overall, the performance of MUSICAv0 and WRF-Chem are similar when compared
684 to the surface CO observations from six WDCGG sites in Africa.

685 (4) Both models have negative bias compared to the MOPITT CO column, especially over
686 Central Africa in September, which is likely driven by fires.

687 (5) Overall, MUSICAv0 agrees better with OMI tropospheric NO₂ column than WRF-
688 Chem.

689 (6) MUSICAv0 overall has a lower tropospheric HCHO column than OMI retrievals in all
690 regions and seasons. Biogenic and fire emissions are likely to be the main driver of this
691 disagreement.

692 (7) Over Africa, the MUSICAv0 simulation has smaller mean bias and RMSE compared
693 to MODIS AOD than the WRF-Chem simulation.

694 (8) The 30°E – 45°E, 5°S – 5°N region in East Africa is potentially a favorable location for
695 future field campaign(s) not only because of the large model-satellite and model-in situ
696 observation discrepancies, but also due to the population density, landcover, and pollution
697 source in this region.

698 Overall, the performance of MUSICAv0 is comparable to WRF-Chem. The
699 underestimation of CO is a common issue in atmospheric chemistry models such as MUSICAv0
700 and WRF-Chem. The overestimation of O₃ in MUSICAv0 is likely driven by too strong of
701 stratosphere-to-troposphere fluxes of O₃ and perhaps an over-estimate of lightning NO emissions,
702 however, future studies are needed to confirm and solve this issue. The significant underestimation
703 in surface PM_{2.5} at two sites in East Africa and the overall overestimation in AOD in Africa
704 compared to MODIS imply missing local sources and an overestimation of dust emissions, and
705 require further study. In addition, lack of data could also contribute to disagreement in model and
706 in situ observations as one site in a city is not representative of the full city. Field campaigns and
707 more in situ observations in 30°E–45°E, 5°S–5°N region in East Africa (as well as other regions
708 in Africa) are necessary for the improvement of atmospheric chemistry model(s) as shown by the
709 MUSICAv0 and WRF-Chem simulations.

710 Fire and dust are important sources of air pollution in Africa. The performance of
711 MUSICAv0 is degraded during fire season and over dust regions. Uncertainties in emission
712 estimates of fire and dust and in the model representation of atmospheric processes could
713 potentially contribute to the model biases. Future studies on fire and dust in Africa are needed to
714 address these uncertainties and air quality modeling over Africa.

715 Here we divided the continent into five sub-regions to show the overall performance of
716 MUSICAv0 over sub-regions of Africa. This accounted for the diversity in atmospheric chemistry
717 environment to some degree. However, each sub-region is not homogeneous. In fact, different
718 cities in the same sub-region may have different emission characteristics. In the future when
719 specific scientific questions are studied with MUSICAv0, we will use higher resolution to address
720 the highly complex and diverse environment. We plan to conduct a model simulation for multiple
721 years and develop additional model grids with potentially higher resolution in Africa sub-regions
722 based on the current MUSICAv0 Africa grid. Higher resolution will benefit the comparisons of
723 model and in situ observations. The future simulation will be conducted for years after 2017 as
724 there are more in situ observations available in recent years.

725

726 **Code and data availability**

727 The model code used here can be accessed through <https://doi.org/10.5281/zenodo.8051435>. The
728 data produced by this study can be accessed through <https://doi.org/10.5281/zenodo.8051443>.

729

730 **Acknowledgement**

731 This material is based upon work partially supported by the National Aeronautics and Space
732 Administration under Grant No. 80NSSC23K0181 issued through the NASA Applied Sciences
733 SERVIR program. We thank ATom, WDCGG, IAGOS, NASA/GSFC SHADOZ teams, and the
734 U.S. State Department and the U.S. EPA for in situ observations. We thank Anne Thompson and
735 Gonzague Romanens for detailed explanation of SHADOZ Ozone data format. We thank
736 MOPITT, MODIS AOD, OMI NO₂ and OMI HCHO teams for the satellite products. The NCAR
737 MOPITT project is supported by the National Aeronautics and Space Administration (NASA)
738 Earth Observing System (EOS) program. We thank the QA4ECV project. We thank Sabine Darras
739 for CAMsv5.1 emissions. We would like to acknowledge high-performance computing support
740 from Cheyenne (doi:10.5065/D6RX99HX) provided by NCAR's Computational and Information
741 Systems Laboratory, sponsored by the National Science Foundation. This material is based upon
742 work supported by the National Center for Atmospheric Research, which is a major facility
743 sponsored by the National Science Foundation under Cooperative Agreement No. 1852977. We
744 thank James Hannigan, Ivan Ortega, Siyuan Wang, and all the attendees of ACOM CAM-
745 chem/MUSICA weekly meeting for helpful discussions.

746

747 **Competing interests**

748 The contact author has declared that neither they nor their co-authors have any competing
749 interests.

750

751 **Author contributions**

752 WT, LKE, HMW, and PL were involved in the initial design of this study. WT led the analysis.
753 RK and CH conducted the WRF-Chem simulation. ZZ interpreted PM_{2.5} results. BG, ST, SM
754 and other coauthors provide discussions. RRB helped with QFED emissions. CG and AS produced
755 CAMsv5.1 emissions. KM, BCD, JP, and CT conducted measurements during ATom. WT
756 prepared the paper with improvements from all coauthors.

757

758

759 **Reference**

760 Archibald, S., Roy, D.P., van Wilgen, B.W. and Scholes, R.J.: What limits fire? An examination
761 of drivers of burnt area in Southern Africa. *Global Change Biology*, 15(3), pp.613-630, 2009.

762 Archibald, S., Scholes, R.J., Roy, D.P., Roberts, G. and Boschetti, L., 2010. Southern African fire
763 regimes as revealed by remote sensing. *International Journal of Wildland Fire*, 19(7), pp.861-878.

764 Archibald, S., 2016. Managing the human component of fire regimes: lessons from Africa.
765 *Philosophical Transactions of the Royal Society B: Biological Sciences*, 371(1696), p.20150346.

- 766 Atuhaire, C., Gidudu, A., Bainomugisha, E. and Mazimwe, A., 2022. Determination of Satellite-
767 Derived PM_{2.5} for Kampala District, Uganda. *Geomatics*, 2(1), pp.125-143.
- 768 Baudoin, M.A., Vogel, C., Nortje, K. and Naik, M., 2017. Living with drought in South Africa:
769 lessons learnt from the recent El Niño drought period. *International journal of disaster risk*
770 *reduction*, 23, pp.128-137.
- 771 Bauer, S. E., Im, U., Mezuman, K., & Gao, C. Y. (2019). Desert dust, industrialization, and
772 agricultural fires: Health impacts of outdoor air pollution in Africa. *Journal of Geophysical*
773 *Research: Atmospheres*, 124, 4104– 4120. <https://doi.org/10.1029/2018JD029336>.
- 774 Boone, A.A., Xue, Y., De Sales, F., Comer, R.E., Hagos, S., Mahanama, S., Schiro, K., Song, G.,
775 Wang, G., Li, S. and Mechoso, C.R., 2016. The regional impact of Land-Use Land-cover Change
776 (LULCC) over West Africa from an ensemble of global climate models under the auspices of the
777 WAMME2 project. *Climate Dynamics*, 47(11), pp.3547-3573.
- 778 Brown, F., Folberth, G. A., Sitch, S., Bauer, S., Bauters, M., Boeckx, P., Cheesman, A. W., Deushi,
779 M., Dos Santos Vieira, I., Galy-Lacaux, C., Haywood, J., Keeble, J., Mercado, L. M., O'Connor,
780 F. M., Oshima, N., Tsigaridis, K., and Verbeeck, H., 2022. The ozone–climate penalty over South
781 America and Africa by 2100, *Atmos. Chem. Phys.*, 22, 12331–12352, [https://doi.org/10.5194/acp-](https://doi.org/10.5194/acp-22-12331-2022)
782 [22-12331-2022](https://doi.org/10.5194/acp-22-12331-2022).
- 783 Boersma, K. F., Eskes, H., Richter, A., De Smedt, I., Lorente, A., Beirle, S., Van Geffen, J., Peters,
784 E., Van Roozendaal, M. and Wagner, T., (2017a). QA4ECV NO₂ tropospheric and stratospheric
785 vertical column data from OMI (Version 1.1). Royal Netherlands Meteorological Institute
786 (KNMI). <http://doi.org/10.21944/qa4ecv-no2-omi-v1.1>.
- 787 Boersma, K.F., van Geffen, J., Eskes, H., van der A, R., De Smedt, I. and Van Roozendaal, M.,
788 2017b. Product specification document for the QA4ECV NO₂ ECV precursor product.
- 789 Bourgeois, I., Peischl, J., Thompson, C. R., Aikin, K. C., Campos, T., Clark, H., Commane, R.,
790 Daube, B., Diskin, G. W., Elkins, J. W., Gao, R.-S., Gaudel, A., Hints, E. J., Johnson, B. J., Kivi,
791 R., McKain, K., Moore, F. L., Parrish, D. D., Querel, R., Ray, E., Sánchez, R., Sweeney, C.,
792 Tarasick, D. W., Thompson, A. M., Thouret, V., Witte, J. C., Wofsy, S. C., and Ryerson, T. B.:
793 Global-scale distribution of ozone in the remote troposphere from the ATom and HIPPO airborne
794 field missions, *Atmos. Chem. Phys.*, 20, 10611–10635, [https://doi.org/10.5194/acp-20-10611-](https://doi.org/10.5194/acp-20-10611-2020)
795 [2020](https://doi.org/10.5194/acp-20-10611-2020), 2020.
- 796 Bourgeois, I., Peischl, J., Neuman, J.A., Brown, S.S., Thompson, C.R., Aikin, K.C., Allen, H.M.,
797 Angot, H., Apel, E.C., Baublitz, C.B. and Brewer, J.F., 2021. Large contribution of biomass
798 burning emissions to ozone throughout the global remote troposphere. *Proceedings of the National*
799 *Academy of Sciences*, 118(52), p.e2109628118.
- 800 Center for International Earth Science Information Network (CIESIN), Columbia University.
801 2018. Documentation for the Gridded Population of the World, Version 4 (GPWv4), Revision 11

802 Data Sets. Palisades NY: NASA Socioeconomic Data and Applications Center (SEDAC).
803 <https://doi.org/10.7927/H45Q4T5F> Accessed 2022-11-17.

804 Chin, M., Ginoux, P., Kinne, S., Torres, O., Holben, B.N., Duncan, B.N., Martin, R.V., Logan,
805 J.A., Higurashi, A., Nakajima, T., 2002. Tropospheric aerosol optical thickness from the GOCART
806 model and comparisons with satellite and sun photometer measurements. *J. Atmos. Sci.* 59, 461–
807 483. [https://doi.org/10.1175/1520-0469\(2002\)059<0461:TAOTFT>2.0.CO;2](https://doi.org/10.1175/1520-0469(2002)059<0461:TAOTFT>2.0.CO;2).

808 Clain, G., Baray, J. L., Delmas, R., Diab, R., Leclair de Bellevue, J., Keckhut, P., Posny, F.,
809 Metzger, J. M., and Cammas, J. P.: Tropospheric ozone climatology at two Southern Hemisphere
810 tropical/subtropical sites, (Reunion Island and Irene, South Africa) from ozonesondes, LIDAR,
811 and in situ aircraft measurements, *Atmos. Chem. Phys.*, 9, 1723–1734,
812 <https://doi.org/10.5194/acp-9-1723-2009>, 2009.

813 Clarke, K., Ash, K., Coker, E.S., Sabo-Attwood, T. and Bainomugisha, E., 2022. A Social
814 Vulnerability Index for Air Pollution and Its Spatially Varying Relationship to PM_{2.5} in Uganda.
815 *Atmosphere*, 13(8), p.1169.

816 Compornolle, S., Verhoelst, T., Pinardi, G., Granville, J., Hubert, D., Keppens, A., Niemeijer, S.,
817 Rino, B., Bais, A., Beirle, S., Boersma, F., Burrows, J. P., De Smedt, I., Eskes, H., Goutail, F.,
818 Hendrick, F., Lorente, A., Pazmino, A., Peters, A., Peters, E., Pommereau, J.-P., Remmers, J.,
819 Richter, A., van Geffen, J., Van Roozendaal, M., Wagner, T., and Lambert, J.-C.: Validation of
820 Aura-OMI QA4ECV NO₂ climate data records with ground-based DOAS networks: the role of
821 measurement and comparison uncertainties, *Atmos. Chem. Phys.*, 20, 8017–8045,
822 <https://doi.org/10.5194/acp-20-8017-2020>, 2020.

823 Darmenov, A., & da Silva, A. (2013). The quick fire emissions dataset (QFED)—documentation of
824 versions 2.1, 2.2 and 2.4. NASA Technical Report Series on Global Modeling and Data
825 Assimilation, NASA TM-2013-104606, 32, 183.

826 Davidson, O., Halsnaes, K., Huq, S., Kok, M., Metz, B., Sokona, Y. and Verhagen, J., 2003. The
827 development and climate nexus: the case of sub-Saharan Africa. *Climate policy*, 3(sup1), pp.S97-
828 S113.

829 De Longueville, F., Hountondji, Y.C., Henry, S. and Ozer, P., 2010. What do we know about
830 effects of desert dust on air quality and human health in West Africa compared to other regions?.
831 *Science of the total environment*, 409(1), pp.1-8.

832 De Smedt, I., Yu, H., Richter, A., Beirle, S., Eskes, H., Boersma, K.F., Van Roozendaal, M., Van
833 Geffen, J., Lorente, A. and Peters, E., (2017a), QA4ECV HCHO tropospheric column data from
834 OMI (Version 1.1). Royal Belgian Institute for Space Aeronomy.
835 <http://doi.org/10.18758/71021031>.

836 De Smedt, I., Van Geffen, J., Richter, A., Beirle S., Yu, H., Vlietinck J., Van Roozendaal, M. van
837 der A R., Lorente A., Scanlon T., Compornolle S., Wagner T., Boersma, K. F., Eskes, H., 2017b,
838 Product User Guide for HCHO.

- 839 Deeter, M.N., 2009. MOPITT (Measurements of Pollution in the Troposphere) Validated Version
840 4 Product User's Guide. National Centre for Atmospheric Research, Boulder, CO, 80307.
- 841 Deeter, M. N., Worden, H. M., Gille, J. C., Edwards, D. P., Mao, D., and Drummond, J. R.:
842 MOPITT multispectral CO retrievals: Origins and effects of geophysical radiance errors, J.
843 Geophys. Res., 116, D15303, <https://doi.org/10.1029/2011JD015703>, 2011.
- 844 Deeter, M., Francis, G., Gille, J., Mao, D., Martínez-Alonso, S., Worden, H., Ziskin, D.,
845 Drummond, J., Commane, R., Diskin, G., and McKain, K.: The MOPITT Version 9 CO product:
846 sampling enhancements and validation, Atmos. Meas. Tech., 15, 2325–2344,
847 <https://doi.org/10.5194/amt-15-2325-2022>, 2022.
- 848 Djossou, J., Léon, J.-F., Akpo, A. B., Lioussé, C., Yoboué, V., Bedou, M., Bodjrenou, M., Chiron,
849 C., Galy-Lacaux, C., Gardrat, E., Abbey, M., Keita, S., Bahino, J., Touré N'Datchoh, E., Ossohou,
850 M., and Awanou, C. N.: Mass concentration, optical depth and carbon composition of particulate
851 matter in the major southern West African cities of Cotonou (Benin) and Abidjan (Côte d'Ivoire),
852 Atmos. Chem. Phys., 18, 6275–6291, <https://doi.org/10.5194/acp-18-6275-2018>, 2018.
- 853 Emmons, L.K., Walters, S., Hess, P.G., Lamarque, J.-F., Pfister, G.G., Fillmore, D., Granier, C.,
854 Guenther, A., Kinnison, D., Laepple, T., Orlando, J., Tie, X., Tyndall, G., Wiedinmyer, C.,
855 Baughcum, S.L., Kloster, S., 2010. Description and evaluation of the model for ozone and related
856 chemical tracers, version 4 (MOZART-4). Geosci. Model Dev. 3, 43–67.
857 <https://doi.org/10.5194/gmd-3-43-2010>.
- 858 Emmons, L.K., Schwantes, R. H., Orlando, J. J., Tyndall, G., Kinnison, D., Lamarque, J.-F., et al.:
859 The Chemistry Mechanism in the Community Earth System Model version 2 (CESM2), Journal
860 of Advances in Modeling Earth Systems, 12, <https://doi.org/10.1029/2019MS001882>, 2020.
- 861 Fisher, J. A., Murray, L. T., Jones, D. B. A., & Deutscher, N. M. (2017). Improved method for
862 linear carbon monoxide simulation and source attribution in atmospheric chemistry models
863 illustrated using GEOS-Chem v9. Geoscientific Model Development, 10, 4129–4144.
864 <https://doi.org/10.5194/gmd-10-4129-2017>.
- 865 Fisher, S., Bellinger, D.C., Cropper, M.L., Kumar, P., Binagwaho, A., Koudenoukpo, J.B., Park,
866 Y., Taghian, G. and Landrigan, P.J., 2021. Air pollution and development in Africa: impacts on
867 health, the economy, and human capital. The Lancet Planetary Health, 5(10), pp.e681-e688.
- 868 Friedl, M., D. Sulla-Menashe. MODIS/Terra+Aqua Land Cover Type Yearly L3 Global 0.05Deg
869 CMG V061. 2022, distributed by NASA EOSDIS Land Processes DAAC,
870 <https://doi.org/10.5067/MODIS/MCD12C1.061>. Accessed 2022-11-17.
- 871 Gaubert, B., Arellano, A. F., Barré, J., Worden, H. M., Emmons, L. K., Tilmes, S., Buchholz, R.
872 R., Vitt, F., Raeder, K., Collins, N., Anderson, J. L., Wiedinmyer, C., Martínez-Alonso, S.,
873 Edwards, D. P., Andreae, M. O., Hannigan, J. W., Petri, C., Strong, K., and Jones, N.: Toward a
874 chemical reanalysis in a coupled chemistry-climate model: An evaluation of MOPITT CO

875 assimilation and its impact on tropospheric composition, *J. Geophys. Res.-Atmos.*, 121, 7310–
876 7343, <https://doi.org/10.1002/2016JD024863>, 2016.

877 Gaubert, B., Emmons, L. K., Raeder, K., Tilmes, S., Miyazaki, K., Arellano Jr., A. F., Elguindi,
878 N., Granier, C., Tang, W., Barré, J., Worden, H. M., Buchholz, R. R., Edwards, D. P., Franke, P.,
879 Anderson, J. L., Saunio, M., Schroeder, J., Woo, J.-H., Simpson, I. J., Blake, D. R., Meinardi, S.,
880 Wennberg, P. O., Crouse, J., Teng, A., Kim, M., Dickerson, R. R., He, H., Ren, X., Pusede, S. E.,
881 and Diskin, G. S.: Correcting model biases of CO in East Asia: impact on oxidant distributions
882 during KORUS-AQ, *Atmos. Chem. Phys.*, 20, 14617–14647, <https://doi.org/10.5194/acp-20->
883 14617-2020, 2020.

884 Gelaro, R., McCarty, W., Suárez, M. J., Todling, R., Molod, A., Takacs, L., et al. (2017). The
885 modern-era retrospective analysis for research and applications, version 2 (MERRA-2). *Journal of*
886 *Climate*, 30(14), 5419-5454.

887 Ginoux, P., Chin, M., Tegen, I., Prospero, J.M., Holben, B., Dubovik, O. and Lin, S.J.: Sources
888 and distributions of dust aerosols simulated with the GOCART model. *Journal of Geophysical*
889 *Research: Atmospheres*, 106(D17), pp.20255-20273, 2001.

890 Gordon, J.N., Bilsback, K.R., Fiddler, M.N., Pokhrel, R.P., Fischer, E.V., Pierce, J.R. and Bililign,
891 S., 2023. The effects of trash, residential biofuel, and open biomass burning emissions on local
892 and transported PM_{2.5} and its attributed mortality in Africa. *GeoHealth*, 7(2), p.e2022GH000673.

893 Güneralp, B., Lwasa, S., Masundire, H., Parnell, S. and Seto, K.C., 2017. Urbanization in Africa:
894 challenges and opportunities for conservation. *Environmental research letters*, 13(1), p.015002.

895 Gwaze, P. and Mashele, S.H.: South African Air Quality Information System (SAAQIS) mobile
896 application tool: Bringing real time state of air quality to South Africans. *Clean Air Journal*, 28(1),
897 pp.3-3, 2018.

898 Haile, G.G., Tang, Q., Sun, S., Huang, Z., Zhang, X. and Liu, X., 2019. Droughts in East Africa:
899 Causes, impacts and resilience. *Earth-science reviews*, 193, pp.146-161.

900 Holben, B.N., Eck, T.F., Slutsker, I.A., Tanré, D., Buis, J.P., Setzer, A., Vermote, E., Reagan, J.A.,
901 Kaufman, Y.J., Nakajima, T. and Lavenu, F.: AERONET—A federated instrument network and
902 data archive for aerosol characterization. *Remote sensing of environment*, 66(1), pp.1-16, 1998.

903 Holben, B.N., Tanré, D., Smirnov, A., Eck, T.F., Slutsker, I., Abuhassan, N., Newcomb, W.W.,
904 Schafer, J.S., Chatenet, B., Lavenu, F.J.J.O.G.R.A. and Kaufman, Y.J.: An emerging ground-based
905 aerosol climatology: Aerosol optical depth from AERONET. *Journal of Geophysical Research:*
906 *Atmospheres*, 106(D11), pp.12067-12097, 2001.

907 Heft-Neal, S., Burney, J., Bendavid, E. and Burke, M., 2018. Robust relationship between air
908 quality and infant mortality in Africa. *Nature*, 559(7713), pp.254-258.

- 909 Hsu, N.C., Jeong, M.J., Bettenhausen, C., Sayer, A.M., Hansell, R., Seftor, C.S., Huang, J. and
910 Tsay, S.C., 2013. Enhanced Deep Blue aerosol retrieval algorithm: The second generation. *Journal*
911 *of Geophysical Research: Atmospheres*, 118(16), pp.9296-9315.
- 912 Jenkins, G. and Gueye, M., 2022. Annual and early summer variability in WRF-CHEM simulated
913 West African PM10 during 1960–2016. *Atmospheric Environment*, 273, p.118957.
- 914 Jo, D.S., Emmons, L.K., Callaghan, P., Tilmes, S., Woo, J.H., Kim, Y., Kim, J., Granier, C., Soulié,
915 A., Doumbia, T. and Darras, S., 2023. Comparison of Urban Air Quality Simulations During the
916 KORUS-AQ Campaign With Regionally Refined Versus Global Uniform Grids in the Multi-Scale
917 Infrastructure for Chemistry and Aerosols (MUSICA) Version 0. *Journal of Advances in Modeling*
918 *Earth Systems*, 15(7), p.e2022MS003458. Klimont, Z., Smith, S.J. and Cofala, J., 2013. The last
919 decade of global anthropogenic sulfur dioxide: 2000–2011 emissions. *Environmental Research*
920 *Letters*, 8(1), p.014003.
- 921 Kalisa, E., Nagato, E.G., Bizuru, E., Lee, K.C., Tang, N., Pointing, S.B., Hayakawa, K., Archer,
922 S.D. and Lacap-Bugler, D.C.: Characterization and risk assessment of atmospheric PM2. 5 and
923 PM10 particulate-bound PAHs and NPAHs in Rwanda, Central-East Africa. *Environmental*
924 *science & technology*, 52(21), pp.12179-12187, 2018.
- 925 Kalisa, E., Kuuire, V. and Adams, M., 2023. Children's exposure to indoor and outdoor black
926 carbon and particulate matter air pollution at school in Rwanda, Central-East Africa.
927 *Environmental Advances*, 11, p.100334.
- 928 Keita, S., Liousse, C., Yoboué, V., Dominutti, P., Guinot, B., Assamoi, E.-M., Borbon, A., Haslett,
929 S. L., Bouvier, L., Colomb, A., Coe, H., Akpo, A., Adon, J., Bahino, J., Doumbia, M., Djossou, J.,
930 Galy-Lacaux, C., Gardrat, E., Gnamien, S., Léon, J. F., Ossouhou, M., N'Datchoh, E. T., and
931 Roblou, L.: Particle and VOC emission factor measurements for anthropogenic sources in West
932 Africa, *Atmos. Chem. Phys.*, 18, 7691–7708, <https://doi.org/10.5194/acp-18-7691-2018>, 2018.
- 933 Keita, S., Liousse, C., Assamoi, E.-M., Doumbia, T., N'Datchoh, E. T., Gnamien, S., Elguindi, N.,
934 Granier, C., and Yoboué, V.: African anthropogenic emissions inventory for gases and particles
935 from 1990 to 2015, *Earth Syst. Sci. Data*, 13, 3691–3705, [https://doi.org/10.5194/essd-13-3691-](https://doi.org/10.5194/essd-13-3691-2021)
936 [2021](https://doi.org/10.5194/essd-13-3691-2021), 2021.
- 937 Kinney, P.L., Gichuru, M.G., Volavka-Close, N., Ngo, N., Ndiba, P.K., Law, A., Gachanja, A.,
938 Gaita, S.M., Chillrud, S.N. and Sclar, E., 2011. Traffic impacts on PM2. 5 air quality in Nairobi,
939 Kenya. *Environmental science & policy*, 14(4), pp.369-378.
- 940 Kuik, F., Lauer, A., Beukes, J. P., Van Zyl, P. G., Josipovic, M., Vakkari, V., Laakso, L., and Feig,
941 G. T.: The anthropogenic contribution to atmospheric black carbon concentrations in southern
942 Africa: a WRF-Chem modeling study, *Atmos. Chem. Phys.*, 15, 8809–8830,
943 <https://doi.org/10.5194/acp-15-8809-2015>, 2015.
- 944 Kumar, R., He, C., Bhardwaj, P., Lacey, F., Buchholz, R.R., Brasseur, G.P., Joubert, W.,
945 Labuschagne, C., Kozlova, E. and Mkololo, T., 2022. Assessment of regional carbon monoxide

- 946 simulations over Africa and insights into source attribution and regional transport. *Atmospheric*
947 *Environment*, 277, p.119075.
- 948 Labuschagne, C., Kuyper, B., Brunke, E.G., Mokolo, T., Van der Spuy, D., Martin, L.,
949 Mbambalala, E., Parker, B., Khan, M.A.H., Davies-Coleman, M.T. and Shallcross, D.E.: A review
950 of four decades of atmospheric trace gas measurements at Cape Point, South Africa. *Transactions*
951 *of the Royal Society of South Africa*, 73(2), pp.113-132, 2018.
- 952 Lacey, F. G., Marais, E. A., Henze, D. K., Lee, C. J., van Donkelaar, A., Martin, R. V., et al. (2017).
953 Improving present day and future estimates of anthropogenic sectoral emissions and the resulting
954 air quality impacts in Africa. *Faraday Discussions*, 200, 397–412.
955 <https://doi.org/10.1039/C7FD00011A>.
- 956 Lamarque, J.F., Bond, T.C., Eyring, V., Granier, C., Heil, A., Klimont, Z., Lee, D., Liousse, C.,
957 Mieville, A., Owen, B. and Schultz, M.G., 2010. Historical (1850–2000) gridded anthropogenic
958 and biomass burning emissions of reactive gases and aerosols: methodology and application.
959 *Atmospheric Chemistry and Physics*, 10(15), pp.7017-7039.
- 960 Langerman, K.E., Garland, R.M., Feig, G., Mpanza, M. and Wernecke, B., 2023. South Africa's
961 electricity disaster is an air quality disaster, too. *Clean Air Journal*, 33(1), pp.1-2.
- 962 Lauritzen, P. H., Nair, R. D., Herrington, A. R., Callaghan, P., Goldhaber, S., Dennis, J. M.,
963 Bacmeister, J. T., Eaton, B. E., Zarzycki, C. M., Taylor, M. A., Ullrich, P. A., Dubos, T., Gettelman,
964 A., Neale, R. B., Dobbins, B., Reed, K. A., Hannay, C., Medeiros, B., Benedict, J. J. and Tribbia,
965 J. J.: NCAR Release of CAM-SE in CESM2.0: A Reformulation of the Spectral Element
966 Dynamical Core in Dry-Mass Vertical Coordinates With Comprehensive Treatment of
967 Condensates and Energy, *Journal of Advances in Modeling Earth Systems*, 10(7), 1537–1570,
968 2018.
- 969 Leclair De Bellevue, J., Réchou, A., Baray, J. L., Ancellet, G., and Diab, R. D.:Signatures of
970 stratosphere to troposphere transport near deep convective events in the southern subtropics, *J.*
971 *Geophys. Res.*, 111, D24107, doi:10.1029/2005JD006947, 2006.
- 972 Levy, R. C., Mattoo, S., Munchak, L. A., Remer, L. A., Sayer, A. M., Patadia, F., and Hsu, N. C.:
973 The Collection 6 MODIS aerosol products over land and ocean, *Atmos. Meas. Tech.*, 6, 2989–
974 3034, <https://doi.org/10.5194/amt-6-2989-2013>, 2013.
- 975 Levy, R., Hsu, C., et al., 2017. MODIS Atmosphere L2 Aerosol Product. NASA MODIS Adaptive
976 Processing System, Goddard Space Flight Center, USA:
977 http://dx.doi.org/10.5067/MODIS/MOD04_L2.061.
- 978 Liousse, C., Assamoi, E., Criqui, P., Granier, C., and Rosset, R.: Explosive growth in African
979 combustion emissions from 2005 to 2030, *Environ. Res. Lett.*, 9, 35003,
980 <https://doi.org/10.1088/1748-9326/9/3/035003>, 2014.

- 981 Liu, J. C., Mickley, L. J., Sulprizio, M. P., Dominici, F., Yue, X., Ebisu, K., ... & Bell, M. L. (2016).
982 Particulate air pollution from wildfires in the Western US under climate change. *Climatic change*,
983 138(3), 655-666.
- 984 Mahowald, N.M., Muhs, D.R., Levis, S., Rasch, P.J., Yoshioka, M., Zender, C.S. and Luo, C.:
985 Change in atmospheric mineral aerosols in response to climate: Last glacial period, preindustrial,
986 modern, and doubled carbon dioxide climates. *Journal of Geophysical Research: Atmospheres*,
987 111(D10), 2006.
- 988 Malings, C., Westervelt, D. M., Haurlyliuk, A., Presto, A. A., Grieshop, A., Bittner, A., Beekmann,
989 M., and R. Subramanian: Application of low-cost fine particulate mass monitors to convert satellite
990 aerosol optical depth to surface concentrations in North America and Africa, *Atmos. Meas. Tech.*,
991 13, 3873–3892, <https://doi.org/10.5194/amt-13-3873-2020>, 2020.
- 992 Marais, E. A., Jacob, D. J., Kurosu, T. P., Chance, K., Murphy, J. G., Reeves, C., Mills, G., Casadio,
993 S., Millet, D. B., Barkley, M. P., Paulot, F., and Mao, J.: Isoprene emissions in Africa inferred
994 from OMI observations of formaldehyde columns, *Atmos. Chem. Phys.*, 12, 6219–6235,
995 <https://doi.org/10.5194/acp-12-6219-2012>, 2012.
- 996 Marais, E.A., Silvern, R.F., Vodonos, A., Dupin, E., Bockarie, A.S., Mickley, L.J. and Schwartz,
997 J., 2019. Air quality and health impact of future fossil fuel use for electricity generation and
998 transport in Africa. *Environmental science & technology*, 53(22), pp.13524-13534.
- 999 Maseko, B., Feig, G. and Burger, R.: Estimating lightning NO_x production over South Africa.
1000 *South African Journal of Science*, 117(9-10), pp.1-11, 2021.
- 1001 Mazzeo, A., Burrow, M., Quinn, A., Marais, E. A., Singh, A., Ng'ang'a, D., Gatari, M. J., and Pope,
1002 F. D.: Evaluation of the WRF and CHIMERE models for the simulation of PM_{2.5} in large East
1003 African urban conurbations, *Atmos. Chem. Phys.*, 22, 10677–10701, <https://doi.org/10.5194/acp-22-10677-2022>, 2022.
- 1005 Menut, L., Flamant, C., Turquety, S., Deroubaix, A., Chazette, P., and Meynadier, R.: Impact of
1006 biomass burning on pollutant surface concentrations in megacities of the Gulf of Guinea, *Atmos.*
1007 *Chem. Phys.*, 18, 2687–2707, <https://doi.org/10.5194/acp-18-2687-2018>, 2018.
- 1008 Mkololo, T., Mbatha, N., Sivakumar, V., Bègue, N., Coetsee, G. and Labuschagne, C.:
1009 Stratosphere–Troposphere exchange and O₃ variability in the lower stratosphere and upper
1010 troposphere over the irene SHADOZ site, South Africa. *Atmosphere*, 11(6), p.586, 2020.
- 1011 Moss, R.H., Brenkert, A.L. and Malone, E.L., 2001. Vulnerability to climate change: a quantitative
1012 approach. Prepared for the US Department of Energy.
- 1013 Naiker, Y., Diab, R.D., Zunckel, M. and Hayes, E.T., 2012. Introduction of local Air Quality
1014 Management in South Africa: overview and challenges. *Environmental science & policy*, 17,
1015 pp.62-71.

- 1016 Nka, B.N., Oudin, L., Karambiri, H., Paturel, J.E. and Ribstein, P., 2015. Trends in floods in West
1017 Africa: Analysis based on 11 catchments in the region. *Hydrology and Earth System Sciences*,
1018 19(11), pp.4707-4719.
- 1019 Nicholson, S.E., 2019. A review of climate dynamics and climate variability in Eastern Africa.
1020 The limnology, climatology and paleoclimatology of the East African lakes, pp.25-56.Okure, D.,
- 1021 Ssematimba, J., Sserunjogi, R., Gracia, N.L., Soppelsa, M.E. and Bainomugisha, E., 2022.
1022 Characterization of ambient air quality in selected urban areas in Uganda using low-cost sensing
1023 and measurement technologies. *Environmental Science & Technology*, 56(6), pp.3324-3339.
- 1024 Oluleye, A. and Okogbue, E.C.: Analysis of temporal and spatial variability of total column ozone
1025 over West Africa using daily TOMS measurements. *Atmospheric Pollution Research*, 4(4),
1026 pp.387-397, 2013.
- 1027 Paton-Walsh, C., Emmerson, K.M., Garland, R.M., Keywood, M., Hoelzemann, J.J., Huneus, N.,
1028 Buchholz, R.R., Humphries, R.S., Altieri, K., Schmale, J. and Wilson, S.R., 2022. Key challenges
1029 for tropospheric chemistry in the Southern Hemisphere. *Elem Sci Anth*, 10(1), p.00050.
- 1030 Petkova, E.P., Jack, D.W., Volavka-Close, N.H. and Kinney, P.L., 2013. Particulate matter
1031 pollution in African cities. *Air Quality, Atmosphere & Health*, 6(3), pp.603-614.
- 1032 Petzold, A., Thouret, V., Gerbig, C., Zahn, A., Brenninkmeijer, C.A., Gallagher, M., Hermann,
1033 M., Pontaud, M., Ziereis, H., Boulanger, D. and Marshall, J., 2015. Global-scale atmosphere
1034 monitoring by in-service aircraft—current achievements and future prospects of the European
1035 Research Infrastructure IAGOS. *Tellus B: Chemical and Physical Meteorology*, 67(1), p.28452.
- 1036 Pfister, G. G., Eastham, S. D., Arellano, A. F., Aumont, B., Barsanti, K. C., Barth, M. C., ... &
1037 Brasseur, G. P. (2020). The Multi-Scale Infrastructure for Chemistry and Aerosols (MUSICA).
1038 *Bulletin of the American Meteorological Society*, 101(10), E1743-E1760.
- 1039 Pokhrel, R.P., Gordon, J., Fiddler, M.N. and Bililign, S., 2021. Determination of emission factors
1040 of pollutants from biomass burning of African fuels in laboratory measurements. *Journal of*
1041 *Geophysical Research: Atmospheres*, 126(20), p.e2021JD034731.
- 1042 Schwantes, R.H., Lacey, F.G., Tilmes, S., Emmons, L.K., Lauritzen, P.H., Walters, S., Callaghan,
1043 P., Zarzycki, C.M., Barth, M.C., Jo, D.S. and Bacmeister, J.T., 2022. Evaluating the impact of
1044 chemical complexity and horizontal resolution on tropospheric ozone over the conterminous US
1045 with a global variable resolution chemistry model. *Journal of Advances in Modeling Earth Systems*,
1046 14(6), p.e2021MS002889.
- 1047 Shindell, D. T., Faluvegi, G., Stevenson, D. S., Krol, M. C., Emmons, L. K., Lamarque, J. F., et
1048 al. (2006). Multimodel simulations of carbon monoxide: Comparison with observations and
1049 projected near-future changes. *Journal of Geophysical Research*, 111.

1050 Soulie, A., C. Granier, S. Darras, N. Zilbermann, T. Doumbia, M. Guevara, J.-P. Jalkanen, S. Keita,
1051 C. Liousse, M. Crippa, D. Guizzardi, R. Hoesly, S. J. Smith, Global Anthropogenic Emissions
1052 (CAM5-GLOB-ANT) for the Copernicus Atmosphere Monitoring Service Simulations of Air
1053 Quality Forecasts and Reanalyses, submitted to Earth Syst. Sci. Data, paper esd-2023-306, 2023.

1054 Stauffer, R.M., Thompson, A.M., Kollonige, D.E., Witte, J.C., Tarasick, D.W., Davies, J., Vömel,
1055 H., Morris, G.A., Van Malderen, R., Johnson, B.J. and Querel, R.R., 2020. A post-2013 dropoff
1056 in total ozone at a third of global ozonesonde stations: Electrochemical concentration cell
1057 instrument artifacts?. *Geophysical Research Letters*, 47(11), p.e2019GL086791.

1058 Stein, O., Schultz, M. G., Bouarar, I., Clark, H., Huijnen, V., Gaudel, A., et al. (2014). On the
1059 wintertime low bias of Northern Hemisphere carbon monoxide found in global model simulations.
1060 *Atmospheric Chemistry and Physics*, 14, 9295–9316.

1061 Swilling, M., Musango, J. and Wakeford, J., 2016. Developmental states and sustainability
1062 transitions: prospects of a just transition in South Africa. *Journal of Environmental Policy &*
1063 *Planning*, 18(5), pp.650-672.

1064 Tang, W., Arellano, A. F., DiGangi, J. P., Choi, Y., Diskin, G. S., Agustí-Panareda, A., Parrington,
1065 M., Massart, S., Gaubert, B., Lee, Y., Kim, D., Jung, J., Hong, J., Hong, J.-W., Kanaya, Y., Lee,
1066 M., Stauffer, R. M., Thompson, A. M., Flynn, J. H., and Woo, J.-H.: Evaluating high-resolution
1067 forecasts of atmospheric CO and CO₂ from a global prediction system during KORUS-AQ field
1068 campaign, *Atmos. Chem. Phys.*, 18, 11007–11030, <https://doi.org/10.5194/acp-18-11007-2018>,
1069 2018.

1070 Tang, W., Emmons, L. K., Arellano Jr., A. F., Gaubert, B., Knote, C., Tilmes, S., Buchholz, R. R.,
1071 Pfister, G. G., Diskin, G. S., Blake, D. R., Blake, N. J., Meinardi, S., DiGangi, J. P., Choi, Y., Woo,
1072 J.-H., He, C., Schroeder, J. R., Suh, I., Lee, H.-J., Jo, H.-Y., Kanaya, Y., Jung, J., Lee, Y., and Kim,
1073 D.: Source contributions to carbon monoxide concentrations during KORUS-AQ based on CAM-
1074 chem model applications, *J. Geophys. Res.-Atmos.*, 124, 1–27,
1075 <https://doi.org/10.1029/2018jd029151>, 2019.

1076 Tang, W., Emmons, L.K., Buchholz, R.R., Wiedinmyer, C., Schwantes, R.H., He, C., Kumar, R.,
1077 Pfister, G.G., Worden, H.M., Hornbrook, R.S. and Apel, E.C., 2022. Effects of Fire Diurnal
1078 Variation and Plume Rise on US Air Quality During FIREX-AQ and WE-CAN Based on the
1079 Multi-Scale Infrastructure for Chemistry and Aerosols (MUSICAv0). *Journal of Geophysical*
1080 *Research: Atmospheres*, 127(16), p.e2022JD036650.

1081 Tang, W., Pfister, G.G., Kumar, R., Barth, M., Edwards, D.P., Emmons, L.K. and Tilmes, S., 2023.
1082 Capturing High-Resolution Air Pollution Features Using the Multi-Scale Infrastructure for
1083 Chemistry and Aerosols Version 0 (MUSICAv0) Global Modeling System. *Journal of*
1084 *Geophysical Research: Atmospheres*, 128(7), p.e2022JD038345.

1085 Taylor, K. E. (2001). Summarizing multiple aspects of model performance in a single diagram.
1086 *Journal of Geophysical Research*, 106(1755), 7183–7192. <https://doi.org/10.1029/2000JD900719>.

1087 Thompson, A. M., Balashov, N. V., Witte, J. C., Coetzee, J. G. R., Thouret, V., and Posny, F.:
1088 Tropospheric ozone increases over the southern Africa region: bellwether for rapid growth in
1089 Southern Hemisphere pollution?, *Atmos. Chem. Phys.*, 14, 9855–9869,
1090 <https://doi.org/10.5194/acp-14-9855-2014>, 2014.

1091 Thompson, A. M., J. C. Witte, C., Sterling, A., Jordan, B. J., Johnson, S. J. Oltmans, ... Thiongo,
1092 K. (2017). First reprocessing of Southern Hemisphere Additional Ozonesondes (SHADOZ) ozone
1093 profiles (1998-2016): 2. Comparisons with satellites and ground-based instruments. *Journal of*
1094 *Geophysical Research: Atmospheres*, 122, 13,000-13,025. <https://doi.org/10.1002/2017JD027406>.

1095 Thompson, C. R., Wofsy, S. C., Prather, M. J., Newman, P. A., Hanisco, T. F., Ryerson, T. B.,
1096 Fahey, D. W., Apel, E. C., Brock, C. A., Brune, W. H., Froyd, K., Katich, J. M., Nicely, J. M.,
1097 Peischl, J., Ray, E., Veres, P. R., Wang, S., Allen, H. M., Asher, E., Bian, H., Blake, D., Bourgeois,
1098 I., Budney, J., Bui, T. P., Butler, A., Campuzano-Jost, P., Chang, C., Chin, M., Commane, R.,
1099 Correa, G., Crouse, J. D., Daube, B., Dibb, J. E., DiGangi, J. P., Diskin, G. S., Dollner, M., Elkins,
1100 J. W., Fiore, A. M., Flynn, C. M., Guo, H., Hall, S. R., Hannun, R. A., Hills, A., Hints, E. J.,
1101 Hodzic, A., Hornbrook, R. S., Huey, L. G., Jimenez, J. L., Keeling, R. F., Kim, M. J., Kupc, A.,
1102 Lacey, F., Lait, L. R., Lamarque, J., Liu, J., McKain, K., Meinardi, S., Miller, D. O., Montzka, S.
1103 A., Moore, F. L., Morgan, E. J., Murphy, D. M., Murray, L. T., Nault, B. A., Neuman, J. A.,
1104 Nguyen, L., Gonzalez, Y., Rollins, A., Rosenlof, K., Sargent, M., Schill, G., Schwarz, J. P., Clair,
1105 J. M. S., Steenrod, S. D., Stephens, B. B., Strahan, S. E., Strode, S. A., Sweeney, C., Thames, A.
1106 B., Ullmann, K., Wagner, N., Weber, R., Weinzierl, B., Wennberg, P. O., Williamson, C. J., Wolfe,
1107 G. M., and Zeng, L.: The NASA Atmospheric Tomography (ATom) Mission: Imaging the
1108 Chemistry of the Global Atmosphere, *B. Am. Meteorol. Soc.*, 103, E761–E790, 2022.

1109 Tilmes, S., Lamarque, J. F., Emmons, L. K., Kinnison, D. E., Ma, P. L., Liu, X., et al. (2015).
1110 Description and evaluation of tropospheric chemistry and aerosols in the Community Earth System
1111 Model (CESM1. 2). *Geoscientific Model Development*, 8, 1395–1426.

1112 Tilmes, S., Hodzic, A., Emmons, L. K., Mills, M. J., Gettelman, A., Kinnison, D. E., et al.: Climate
1113 forcing and trends of organic aerosols in the Community Earth System Model (CESM2). *Journal*
1114 *of Advances in Modeling Earth Systems*, 11, <https://doi.org/10.1029/2019MS001827>, 2019.

1115 Tshela, C. and Wright, C.Y.: 15 years after the National Environmental Management Air Quality
1116 Act: Is legislation failing to reduce air pollution in South Africa?. *South African Journal of Science*,
1117 115(9-10), pp.1-4, 2019.

1118 U.S. EPA: Quality Assurance Guidance Document 2.12: Monitoring PM2.5 in Ambient Air Using
1119 Designated Reference or Class I Equivalent Methods, United States Environmental Protection
1120 Agency, available at: <https://www3.epa.gov/ttnamti1/files/ambient/pm25/qa/m212.pdf> (last
1121 access: 20 November 2022), 2016.

1122 van der Werf, G. R., Randerson, J. T., Giglio, L., van Leeuwen, T. T., Chen, Y., Rogers, B. M.,
1123 Mu, M., van Marle, M. J. E., Morton, D. C., Collatz, G. J., Yokelson, R. J., and Kasibhatla, P. S.,
1124 2017. Global fire emissions estimates during 1997–2016, *Earth Syst. Sci. Data*, 9, 697–720,
1125 <https://doi.org/10.5194/essd-9-697-2017>.

- 1126 Vohra, K., Marais, E.A., Bloss, W.J., Schwartz, J., Mickley, L.J., Van Damme, M., Clarisse, L.
1127 and Coheur, P.F., 2022. Rapid rise in premature mortality due to anthropogenic air pollution in
1128 fast-growing tropical cities from 2005 to 2018. *Science Advances*, 8(14), p.eabm4435.
- 1129 Washington, R., Harrison, M., Conway, D., Black, E., Challinor, A., Grimes, D., Jones, R., Morse,
1130 A., Kay, G. and Todd, M., 2006. African climate change: taking the shorter route. *Bulletin of the*
1131 *American Meteorological Society*, 87(10), pp.1355-1366.
- 1132 Watson, J. G., Chow, J. C., Moosmüller, H., Green, M., Frank, N., and Pitchford, M.: Guidance
1133 for using continuous monitors in PM_{2.5} monitoring networks, U.S. EPA Office of Air Quality
1134 Planning and Standards, Triangle Park, NC., 1998.
- 1135 Wiedinmyer, C., Akagi, S.K., Yokelson, R.J., Emmons, L.K., Al-Saadi, J.A., Orlando, J.J., Soja,
1136 A.J., 2011. The Fire INventory from NCAR (FINN): a high resolution global model to estimate
1137 the emissions from open burning. *Geosci. Model Dev.* 4, 625–641. [https://doi.org/10.5194/gmd-](https://doi.org/10.5194/gmd-4-625-2011)
1138 [4-625-2011](https://doi.org/10.5194/gmd-4-625-2011).
- 1139 Wiedinmyer, C., Yokelson, R. J., and Gullett, B. K.: Global emissions of trace gases, particulate
1140 matter, and hazardous air pollutants from open burning of domestic waste, *Environ. Sci. Technol.*,
1141 48, 9523–9530, <https://doi.org/10.1021/es502250z>, 2014.
- 1142 Witte, J.C., A. M. Thompson, H. G. J. Smit, M. Fujiwara, F. Posny, Gert J. R. Coetzee, ... F. R. da
1143 Silva (2017), First reprocessing of Southern Hemisphere ADDitional OZonesondes (SHADOZ)
1144 profile records (1998-2015): 1. Methodology and evaluation, *J. Geophys. Res. Atmos.*, 122, 6611-
1145 6636. <https://doi.org/10.1002/2016JD026403>.
- 1146 Witte, J. C., Thompson, A. M., Smit, H. G. J., Vömel, H., Posny, F., & Stübi, R. (2018). First
1147 reprocessing of Southern Hemisphere ADDitional OZonesondes profile records: 3. Uncertainty in
1148 ozone profile and total column. *Journal of Geophysical Research: Atmospheres*, 123, 3243-3268.
1149 <https://doi.org/10.1002/2017JD027791>.
- 1150 Wofsy, S.C., S. Afshar, H.M. Allen, E.C. Apel, E.C. Asher, B. Barletta, J. Bent, H. Bian, B.C.
1151 Biggs, D.R. Blake, N. Blake, I. Bourgeois, C.A. Brock, W.H. Brune, J.W. Budney, T.P. Bui, A.
1152 Butler, P. Campuzano-Jost, C.S. Chang, M. Chin, R. Commane, G. Correa, J.D. Crouse, P. D.
1153 Cullis, B.C. Daube, D.A. Day, J.M. Dean-Day, J.E. Dibb, J.P. DiGangi, G.S. Diskin, M. Dollner,
1154 J.W. Elkins, F. Erdesz, A.M. Fiore, C.M. Flynn, K.D. Froyd, D.W. Gesler, S.R. Hall, T.F. Hanisco,
1155 R.A. Hannun, A.J. Hills, E.J. Hints, A. Hoffman, R.S. Hornbrook, L.G. Huey, S. Hughes, J.L.
1156 Jimenez, B.J. Johnson, J.M. Katich, R.F. Keeling, M.J. Kim, A. Kupc, L.R. Lait, K. McKain, R.J.
1157 McLaughlin, S. Meinardi, D.O. Miller, S.A. Montzka, F.L. Moore, E.J. Morgan, D.M. Murphy,
1158 L.T. Murray, B.A. Nault, J.A. Neuman, P.A. Newman, J.M. Nicely, X. Pan, W. Paplawsky, J.
1159 Peischl, M.J. Prather, D.J. Price, E.A. Ray, J.M. Reeves, M. Richardson, A.W. Rollins, K.H.
1160 Rosenlof, T.B. Ryerson, E. Scheuer, G.P. Schill, J.C. Schroder, J.P. Schwarz, J.M. St.Clair, S.D.
1161 Steenrod, B.B. Stephens, S.A. Strode, C. Sweeney, D. Tanner, A.P. Teng, A.B. Thames, C.R.
1162 Thompson, K. Ullmann, P.R. Veres, N.L. Wagner, A. Watt, R. Weber, B.B. Weinzierl, P.O.
1163 Wennberg, C.J. Williamson, J.C. Wilson, G.M. Wolfe, C.T. Woods, L.H. Zeng, and N. Vieznor.

1164 2021. ATom: Merged Atmospheric Chemistry, Trace Gases, and Aerosols, Version 2. ORNL
1165 DAAC, Oak Ridge, Tennessee, USA. <https://doi.org/10.3334/ORNLDAAC/1925>.

1166 Worden, H. M., Deeter, M. N., Edwards, D. P., Gille, J. C., Drummond, J. R., and Nédélec, P.:
1167 Observations of near-surface carbon monoxide from space using MOPITT multispectral retrievals,
1168 *J. Geophys. Res.*, 115, D18314, <https://doi.org/10.1029/2010JD014242>, 2010.

1169 Yoshioka, M., Mahowald, N.M., Conley, A.J., Collins, W.D., Fillmore, D.W., Zender, C.S. and
1170 Coleman, D.B.: Impact of desert dust radiative forcing on Sahel precipitation: Relative importance
1171 of dust compared to sea surface temperature variations, vegetation changes, and greenhouse gas
1172 warming. *Journal of Climate*, 20(8), pp.1445-1467, 2007.

1173 Zhang, D., Du, L., Wang, W., Zhu, Q., Bi, J., Scovronick, N., Naidoo, M., Garland, R.M. and Liu,
1174 Y. A machine learning model to estimate ambient PM_{2.5} concentrations in industrialized highveld
1175 region of South Africa. *Remote sensing of environment*, 266, p.112713, 2021.

1176 Ziervogel, G., New, M., Archer van Garderen, E., Midgley, G., Taylor, A., Hamann, R., Stuart-
1177 Hill, S., Myers, J. and Warburton, M., 2014. Climate change impacts and adaptation in South
1178 Africa. *Wiley Interdisciplinary Reviews: Climate Change*, 5(5), pp.605-620.

1179

1180

1181

1182

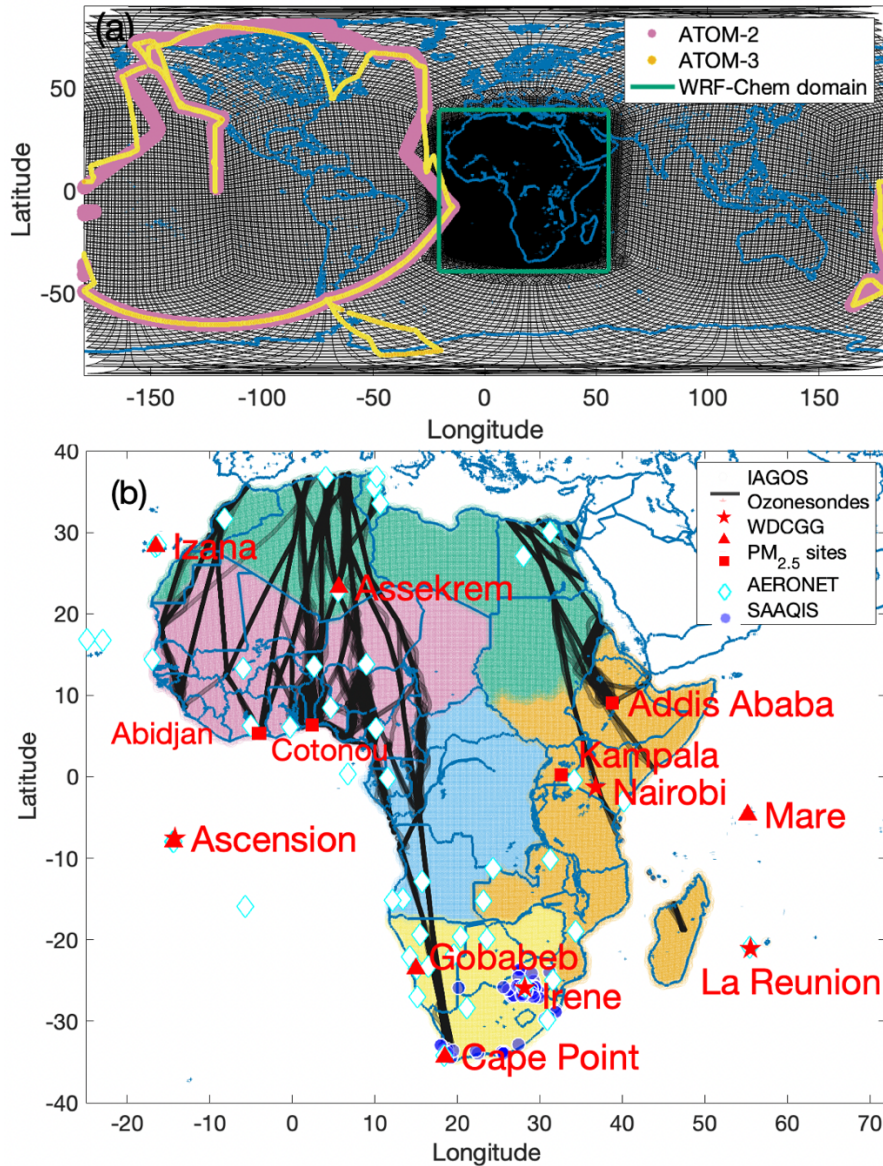
1183

1184

1185

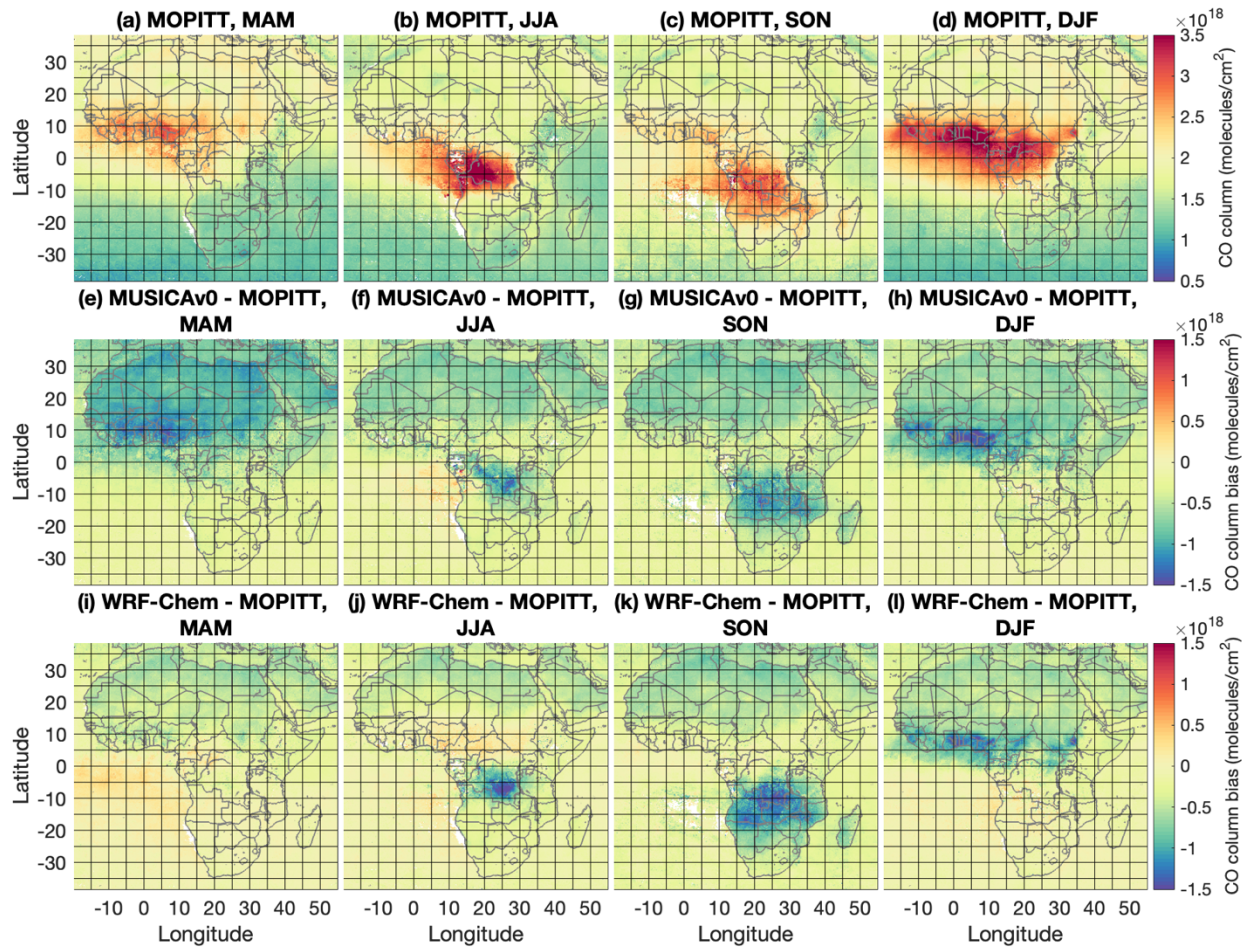
1186

1187



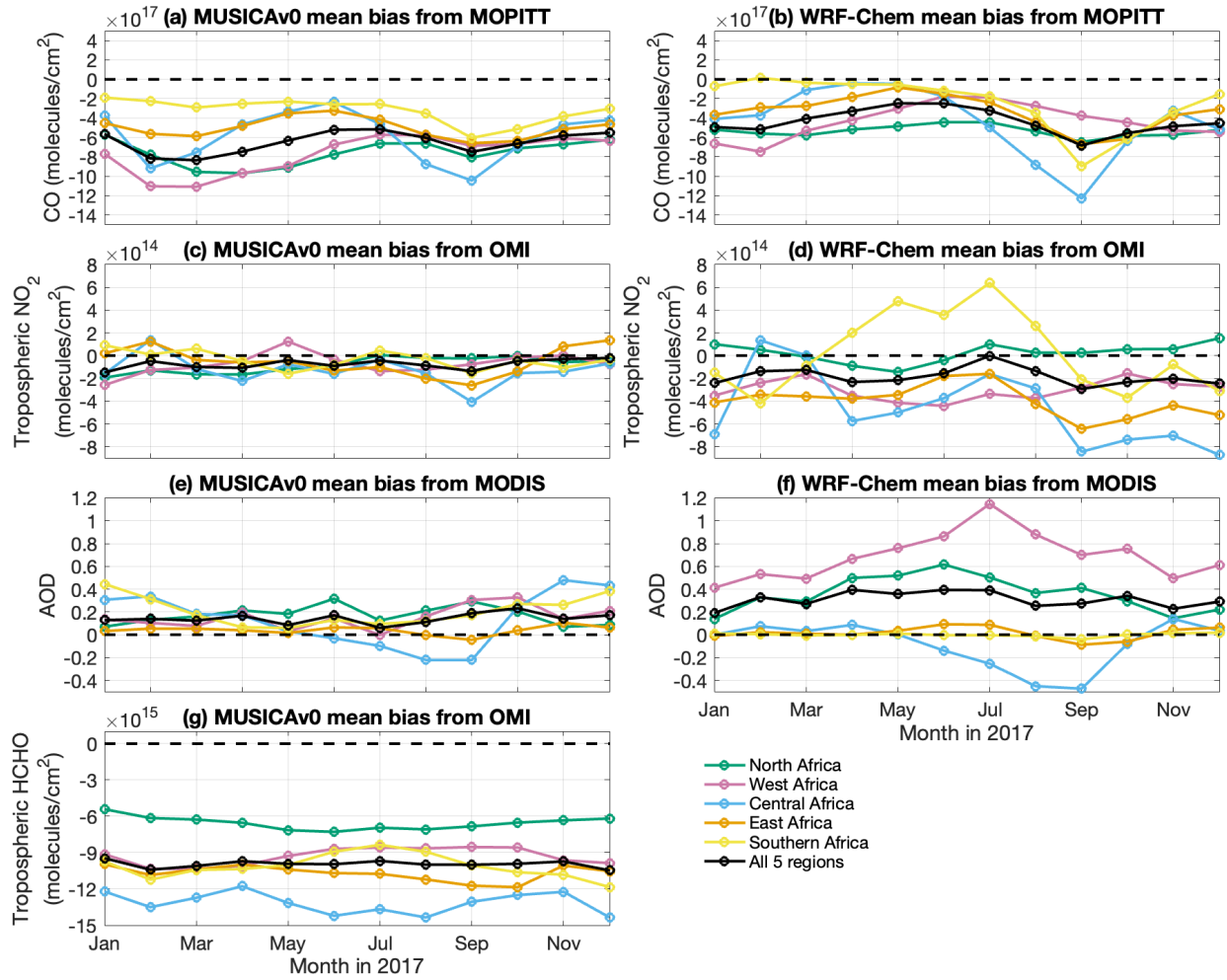
1188
 1189 **Figure 1.** Model grid, in situ observations used in this study, and sub-regions in Africa. (a)
 1190 MUSICA v0 model grid developed for Africa in this study (black), domain boundary of the WRF-
 1191 Chem simulation compared in this study (shown by green box), observations from the
 1192 Atmospheric Tomography Mission (ATom) field campaign 2 (ATom-2; 2017 Jan to 2017 Feb;
 1193 pink) and ATom-3 (2017 Sep to 2017 Oct; yellow). (b) Sub-regions in Africa are shown, namely
 1194 North Africa (green), West Africa (pink), East Africa (orange), Central Africa (blue), and Southern
 1195 Africa (yellow). Location of in situ observations are labeled on the map. Flight tracks of the In-
 1196 service Aircraft for a Global Observing System (IAGOS) are shown with black lines. Four
 1197 ozonesonde sites are shown by pentagrams (Ascension, Irene, Nairobi, and La Reunion); six sites
 1198 from the World Data Centre for Greenhouse Gases are shown by triangles (Assekrem, Cape Point,
 1199 Izana, Gobabeb, Mare, and Ascension); surface sites for PM_{2.5} are shown by squares (Addis Ababa
 1200 and Kampala in East Africa; Abidjan and Cotonou in West Africa); AEROSOL ROBOTIC NETWORK
 1201 (AERONET) sites are shown with diamond; South Africa Air Quality Information System
 1202 (SAAQIS) sites are shown with blue circles.

1203
1204
1205
1206



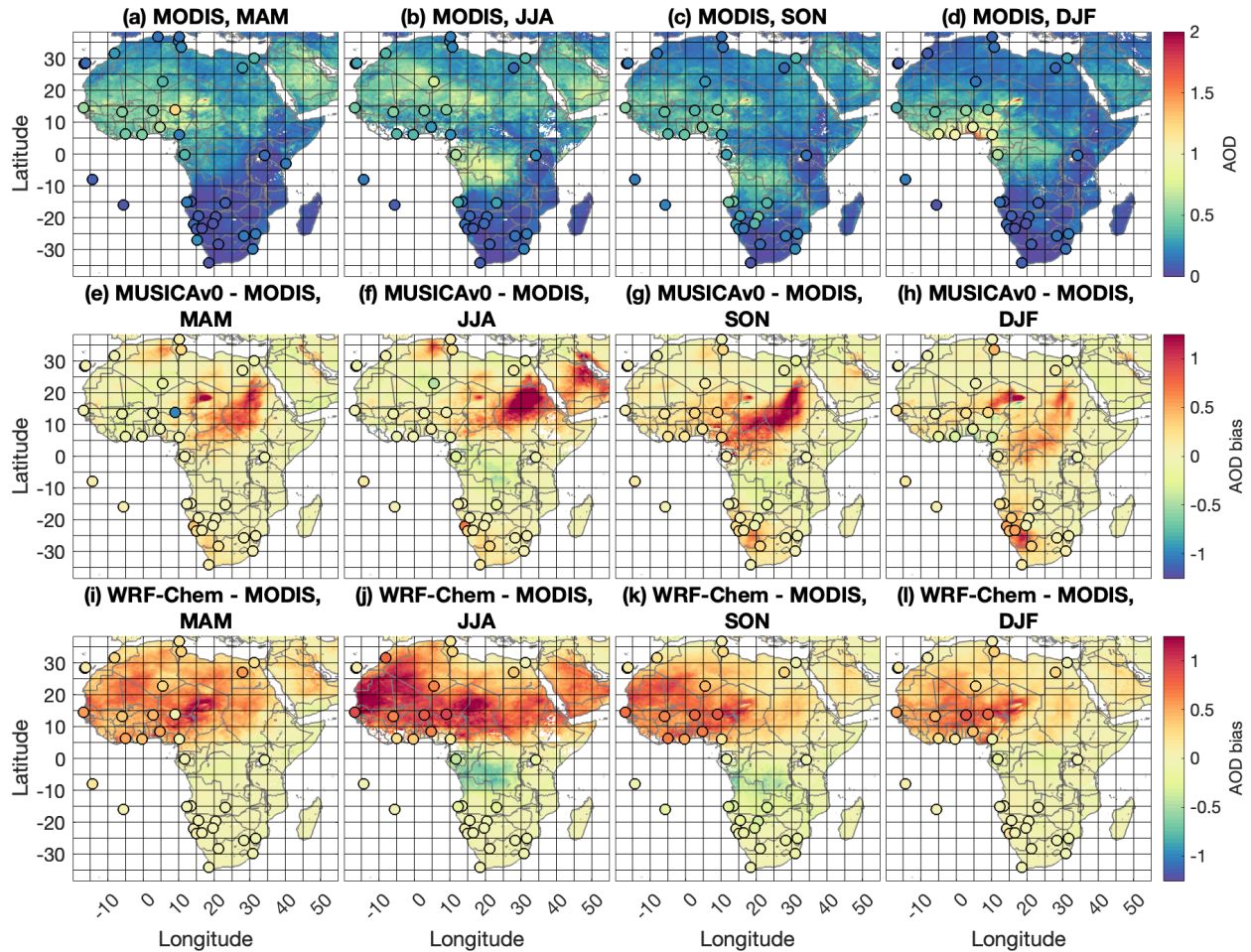
1207
1208
1209
1210
1211
1212
1213
1214
1215

Figure 2. Comparisons of MUSICA v0 and WRF-Chem simulations to MOPITT CO column (molecules/cm²) for each season of 2017. (a-d) Averaged MOPITT CO column: MAM (March, April, and May), JJA (June, July, and August), SON (September, October, and November), and DJF (December, January, and February). (e-h) MUSICA v0 model biases against MOPITT CO column for MAM, JJA, SON, and DJF. (i-l) is the same as (e-h) but for WRF-Chem. All data are gridded to 0.25 degree \times 0.25 degree for plotting.



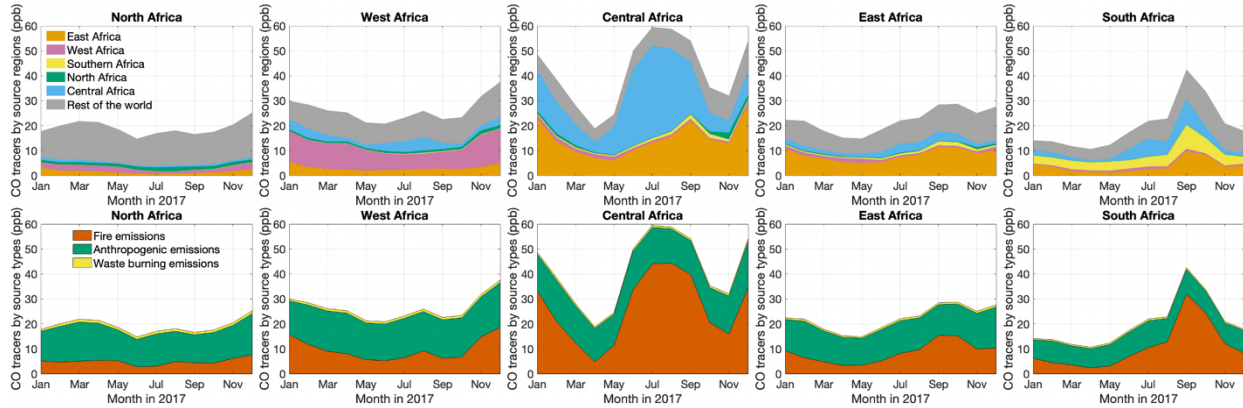
1216
 1217
 1218
 1219
 1220
 1221
 1222
 1223
 1224
 1225

Figure 3. Mean bias of MUSICAv0 and WRF-Chem simulations from satellite data. Monthly timeseries of mean bias of (a) MUSICAv0 and (b) WRF-Chem against MOPITT CO column (molecules/cm²) in 2017 over Africa (black), North Africa (green), West Africa (pink), East Africa (orange), Central Africa (blue), and Southern Africa (yellow). (c-d) are same as (a-b) but for mean bias against OMI tropospheric NO₂ column (molecules/cm²). (e-f) are same as (a-b) but for mean bias against with MODIS (Terra) Aerosol Optical Depth (AOD). (g) is the same as (a) but for mean bias against OMI tropospheric HCHO column (molecules/cm²).

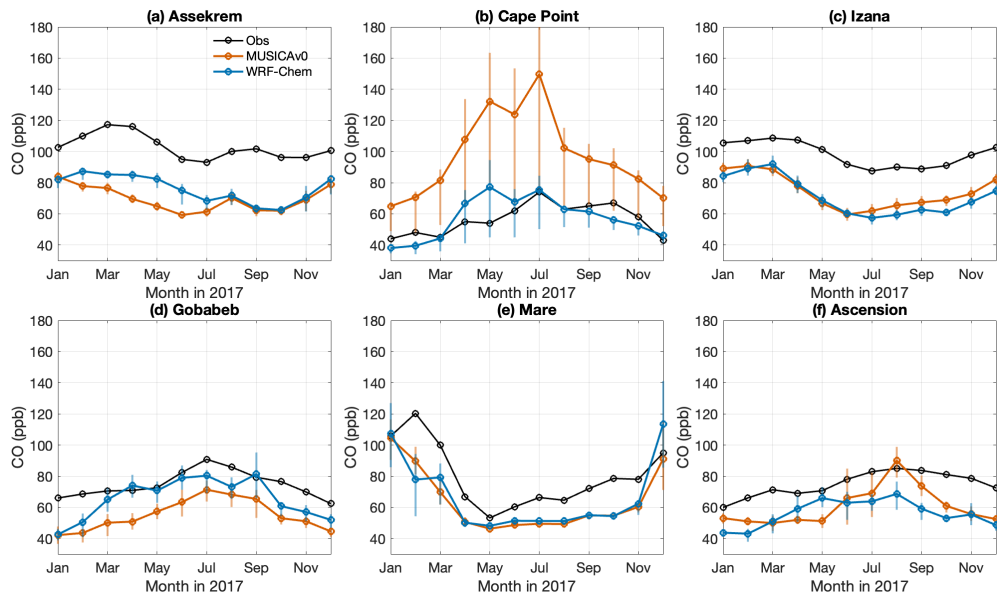


1226
 1227
 1228
 1229
 1230
 1231
 1232
 1233
 1234
 1235
 1236
 1237
 1238
 1239

Figure 4. Comparisons of MUSICAv0 and WRF-Chem simulations and MODIS and AERONET AOD at 550 nm in 2017. (a-d) Averaged MODIS and AERONET AOD in MAM (March, April, and May), JJA (June, July, and August), SON (September, October, and November), and DJF (December, January, and February). (e-h) MUSICAv0 model biases against MODIS and AERONET AOD in MAM, JJA, SON, and DJF. (i-l) is the same as (e-h) but for WRF-Chem. All data are gridded to 0.25 degree \times 0.25 degree for plotting. AERONET AOD in (a-d) and model bias against AERONET AOD in (e-l) are shown by the circles overlaid on the map.

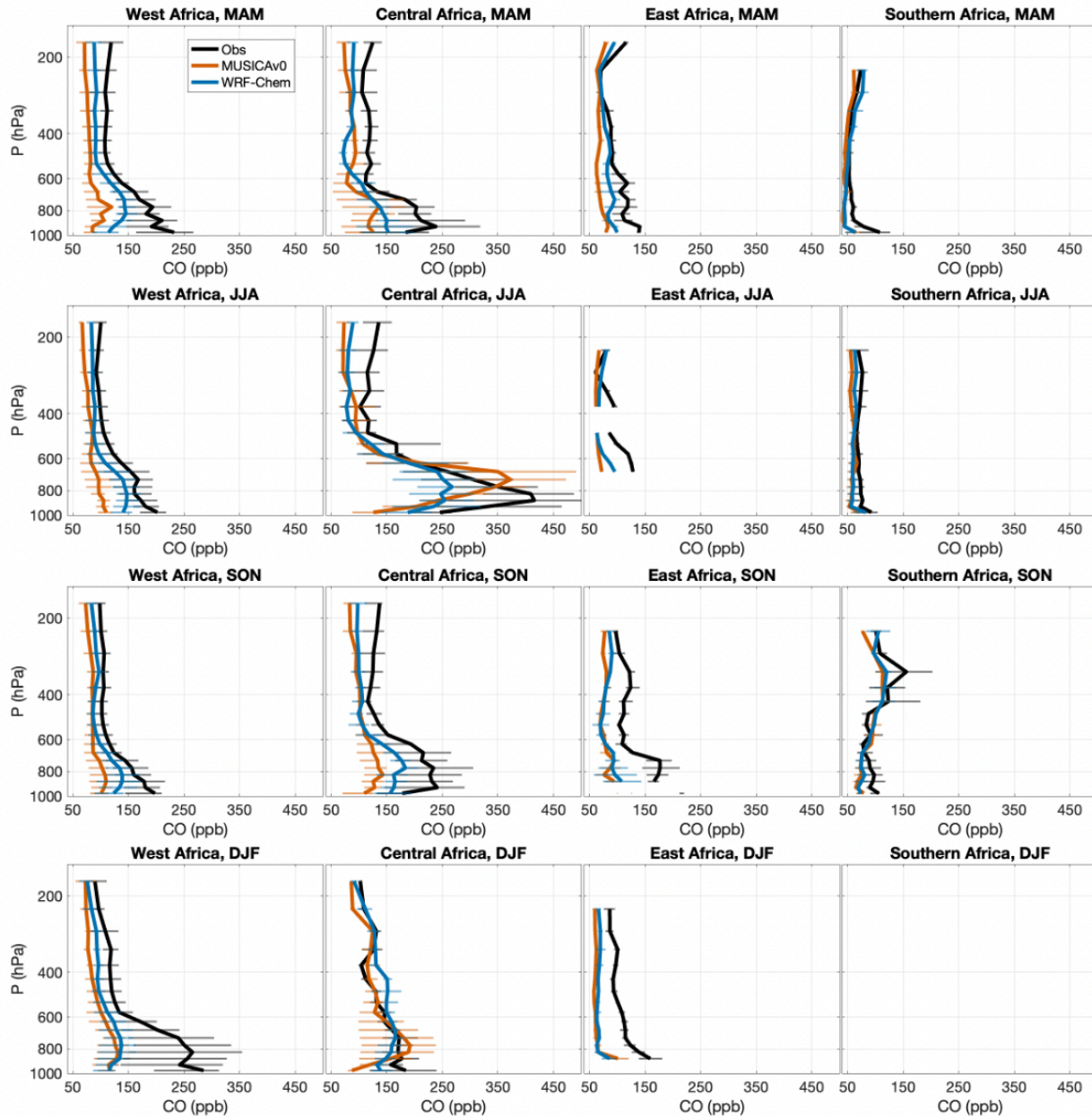


1240
 1241 **Figure 5.** Monthly time series of column-averaged CO tracers in North Africa, West Africa, East
 1242 Africa, Central Africa, and Southern Africa. Top panels show CO tracers of emissions from North
 1243 Africa (green), West Africa (pink), East Africa (orange), Central Africa (blue), Southern Africa
 1244 (yellow), and the rest of the world (grey). Bottom panels show CO tracers of fire emissions (red),
 1245 anthropogenic emissions (green), and waste burning emissions (yellow).
 1246
 1247



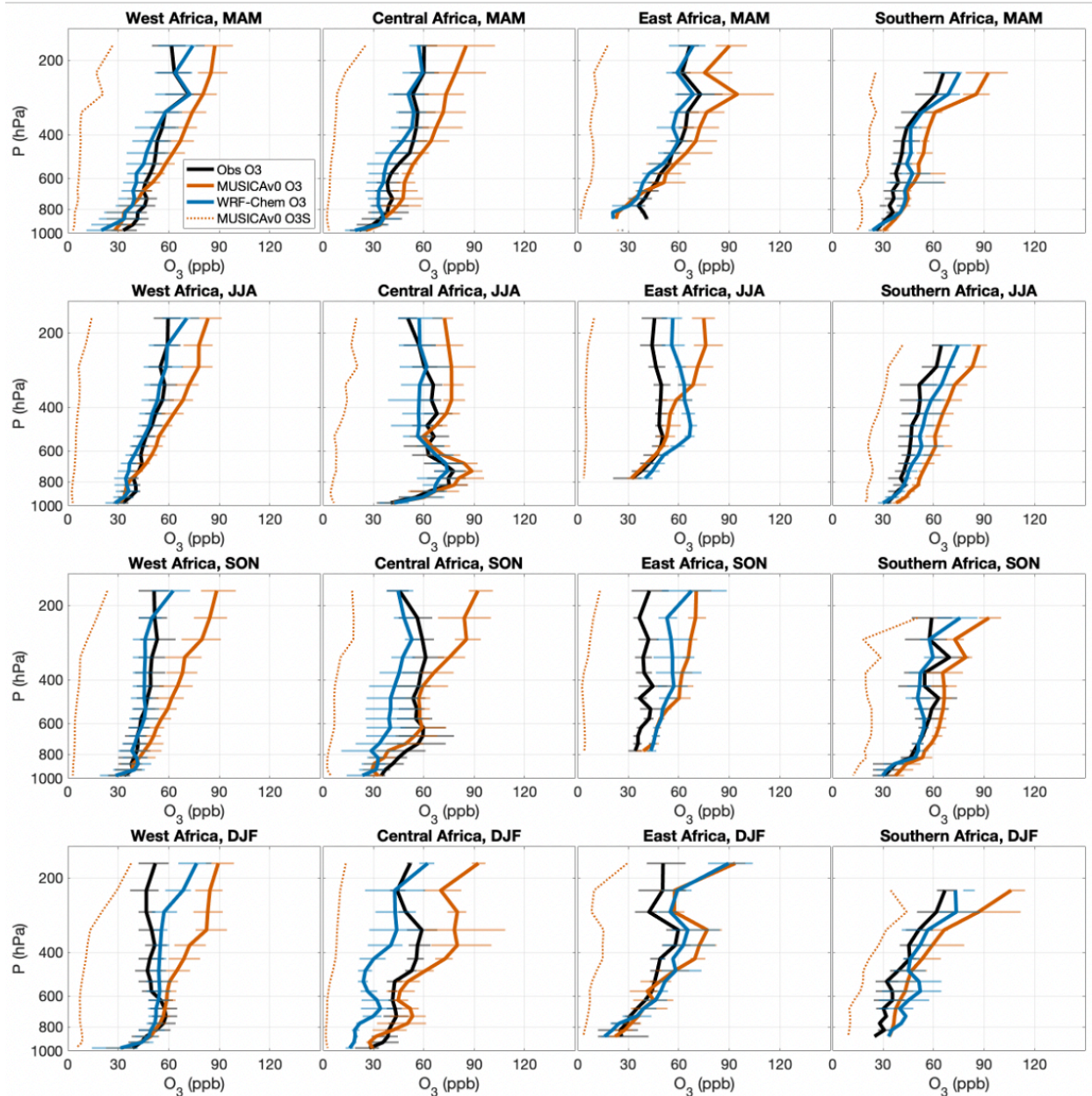
1248
 1249 **Figure 6.** Monthly mean CO (ppb) from in situ observations (black), MUSICA v0 (red), and WRF-
 1250 Chem (blue) during 2017 at (a) Assekrem, (b) Cape Point, (c) Izana, (d) Gobabeb, (e) Mare and
 1251 (f) Ascension (see Figure 1b for locations). Monthly means are calculated from 3-hourly data. The
 1252 range for each data point shows the variation of the 3-hourly data on that day (25% quantile to
 1253 75% quantile). Observational data are from World Data Centre for Greenhouse Gases (WDCGG).
 1254

1255
1256

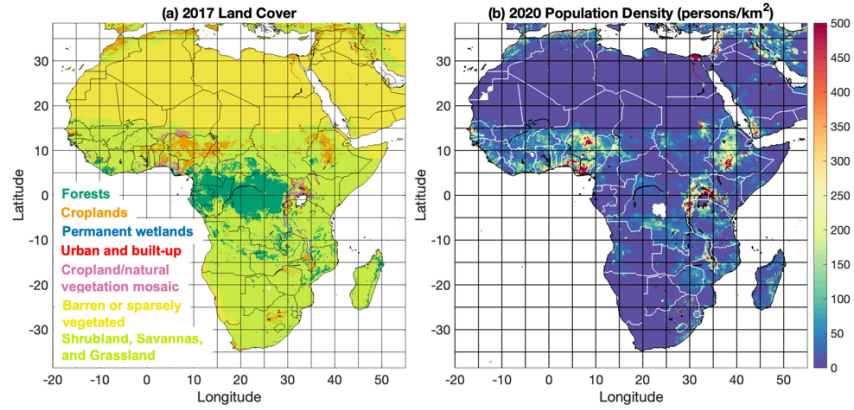


1257
1258
1259
1260
1261
1262
1263
1264
1265

Figure 7. Vertical profiles of CO (ppb) from the In-service Aircraft for a Global Observing System (IAGOS) measurements (black) and corresponding model output from MUSICAv0 (red), and WRF-Chem (blue) during different seasons in 2017 over West Africa, Central Africa, East Africa, and Southern Africa. North Africa is not shown due to data availability. Seasonal mean profiles with the variation of the data in the pressure layer (25% quantile to 75% quantile) in MAM (March, April, and May), JJA (June, July, and August), SON (September, October, and November), and DJF (December, January, and February) are shown.

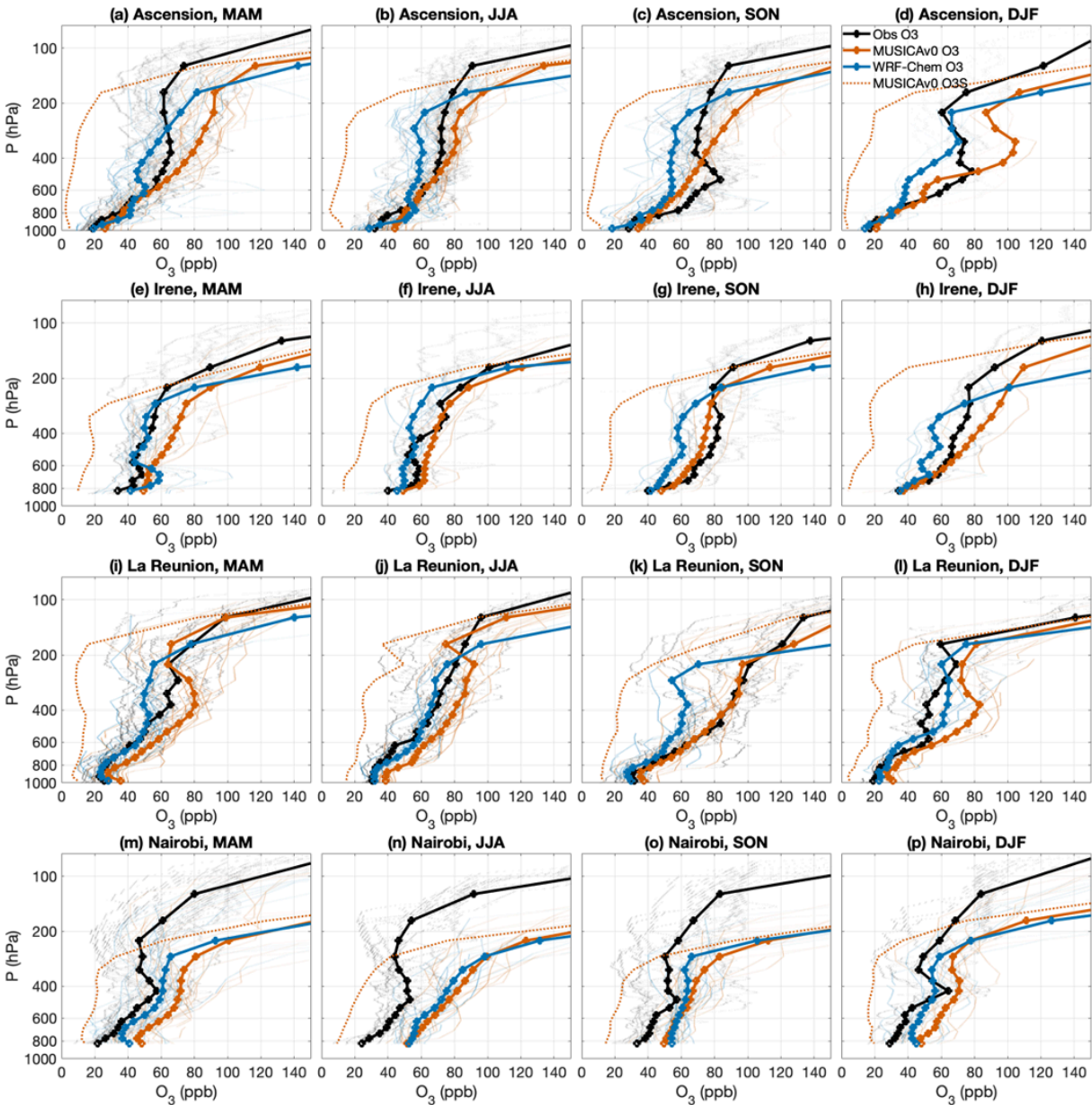


1266
 1267 **Figure 8.** Vertical profiles of O₃ (ppb) from the In-service Aircraft for a Global Observing System
 1268 (IAGOS) measurements (black) and corresponding model output from MUSICAv0 (red), and
 1269 WRF-Chem (blue) during different seasons in 2017 over West Africa, Central Africa, East Africa,
 1270 and Southern Africa. North Africa is not shown due to data availability Seasonal mean profiles
 1271 with the variation of the data in the pressure layer (25% quantile to 75% quantile) in MAM (March,
 1272 April, and May), JJA (June, July, and August), SON (September, October, and November), and
 1273 DJF (December, January, and February) are shown. The dash red lines represent O3S
 1274 (stratospheric ozone tracer) from the MUSICAv0 simulation.

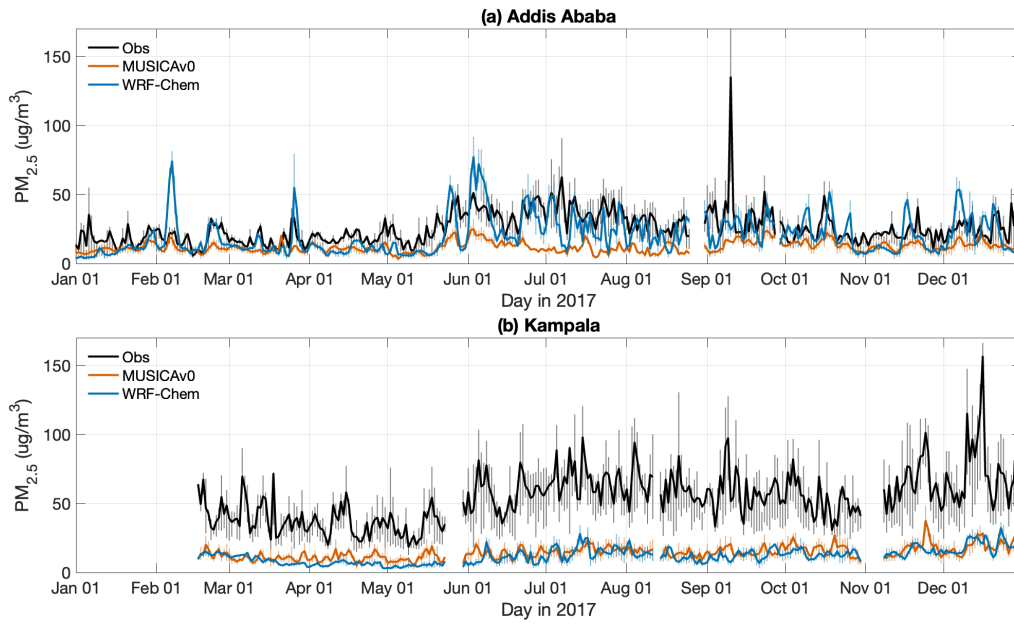


1275
 1276 **Figure 9.** (a) Land cover in 2017 and (b) population density (persons/km²) in 2020 over Africa.
 1277 Land cover data is from MODIS/Terra+Aqua Land Cover Type Yearly L3 Global product
 1278 (resolution: 0.05 degree) (Friedl et al., 2022). Cropland/Natural Vegetation Mosaics means
 1279 Mosaics of small-scale cultivation (40-60%) with natural tree, shrub, or herbaceous vegetation.
 1280 Population density data is from the Gridded Population of the World, Version 4 (GPWv4),
 1281 Revision 11 (CIESIN, 2018).

1282
 1283

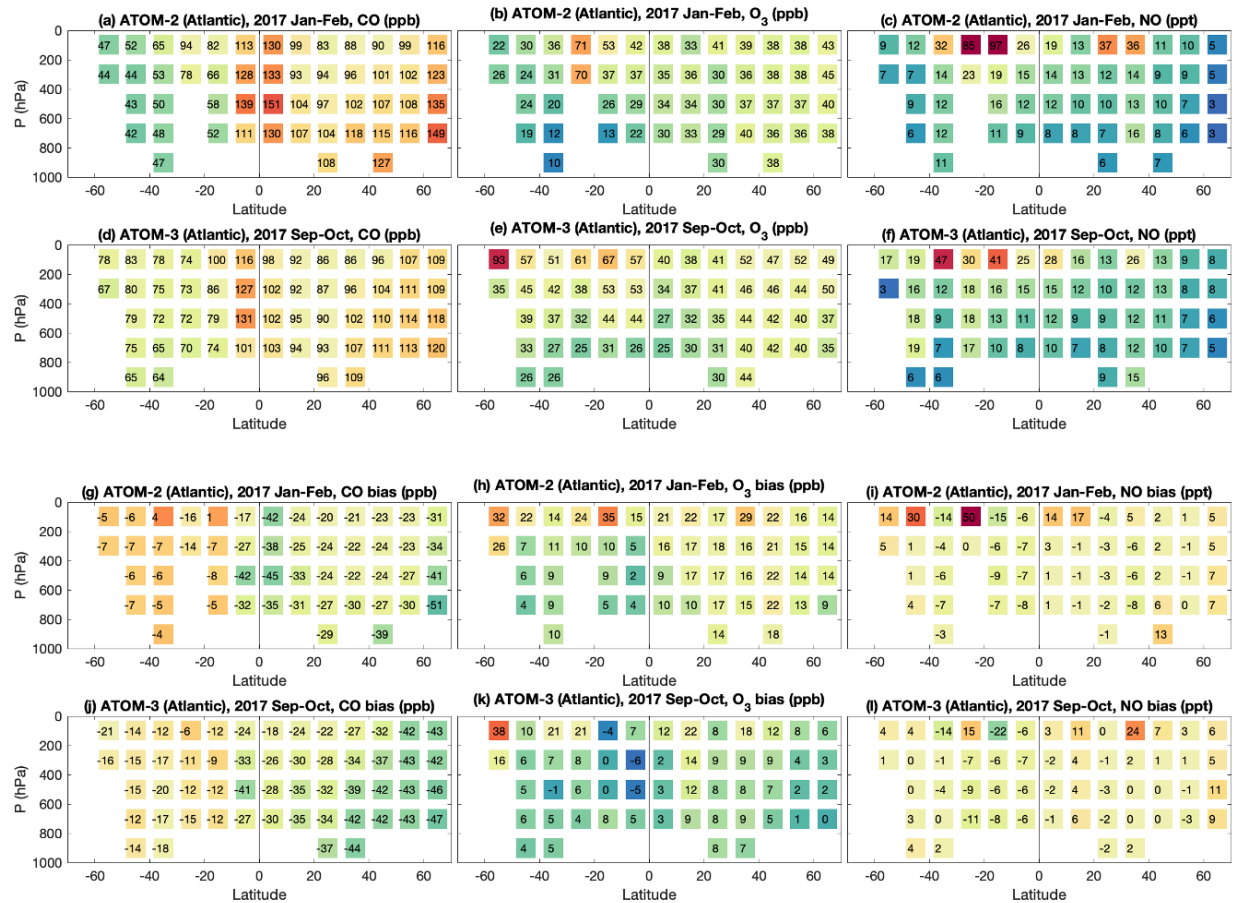


1284
 1285 **Figure 10.** Vertical profiles of O₃ (ppb) from Ozonesondes (black) and corresponding model
 1286 output from MUSICAv0 (red), and WRF-Chem (blue) for each season of 2017. The thick lines
 1287 denote the seasonal mean profiles and the thin lines denote the individual profiles. The dash red
 1288 lines represent O₃S (stratospheric ozone tracer) from the MUSICAv0 simulation. Ozonesonde data
 1289 at Ascension in (a) MAM (March, April, and May), (b) JJA (June, July, and August), (c) SON
 1290 (September, October, and November), and (d) DJF (December, January, and February) are shown.
 1291 (e-h), (i-l), and (m-p) are the same as (a-d), except for Irene, La Reunion, and Nairobi, respectively.
 1292 Locations of the sites are shown in Figure 1b.
 1293



1294
 1295
 1296
 1297
 1298
 1299
 1300

Figure 11. Daily mean $PM_{2.5}$ from in situ observations (black), MUSICAv0 (red), and WRF-Chem (blue) during 2017 at (a) Addis Ababa and (b) Kampala. Daily means are calculated from 3-hourly data. The shown range for each data point shows the variation on that day (25% quantile to 75% quantile). Locations of the sites are shown in Figure 1b.



1301
 1302 **Figure 12.** Observations of (a) CO (ppb), (b) O₃ (ppb), and (c) NO (ppt) over Atlantic Ocean
 1303 during ATom-2 and ATom-3 (d-f). (g-l) corresponding model biases against ATOM observations.
 1304 The ATom airborne measurements and corresponding MUSICA v0 model results are binned to 10-
 1305 degree latitude and 200-hPa pressure bins. The values of mean biases for each latitude and pressure
 1306 bin are labeled in the figure.
 1307

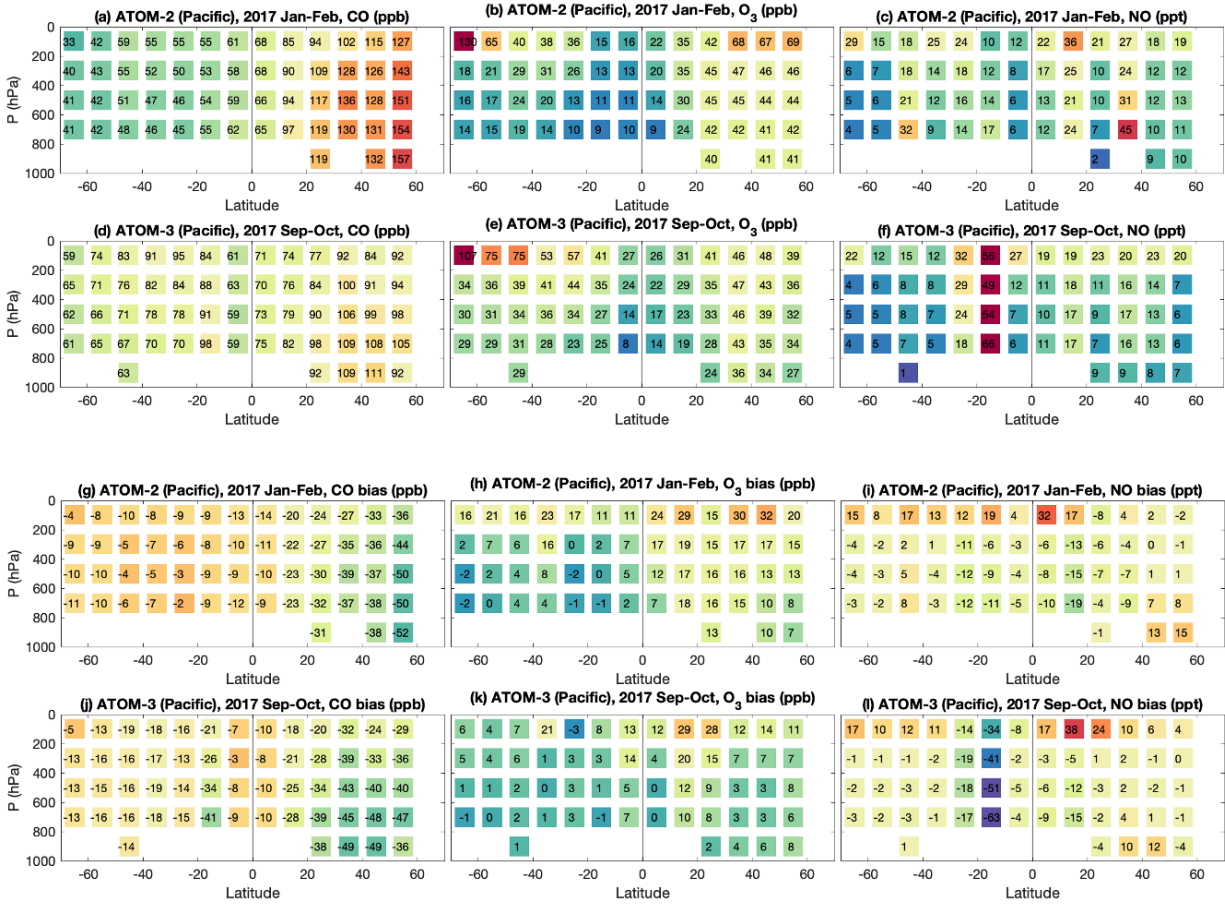
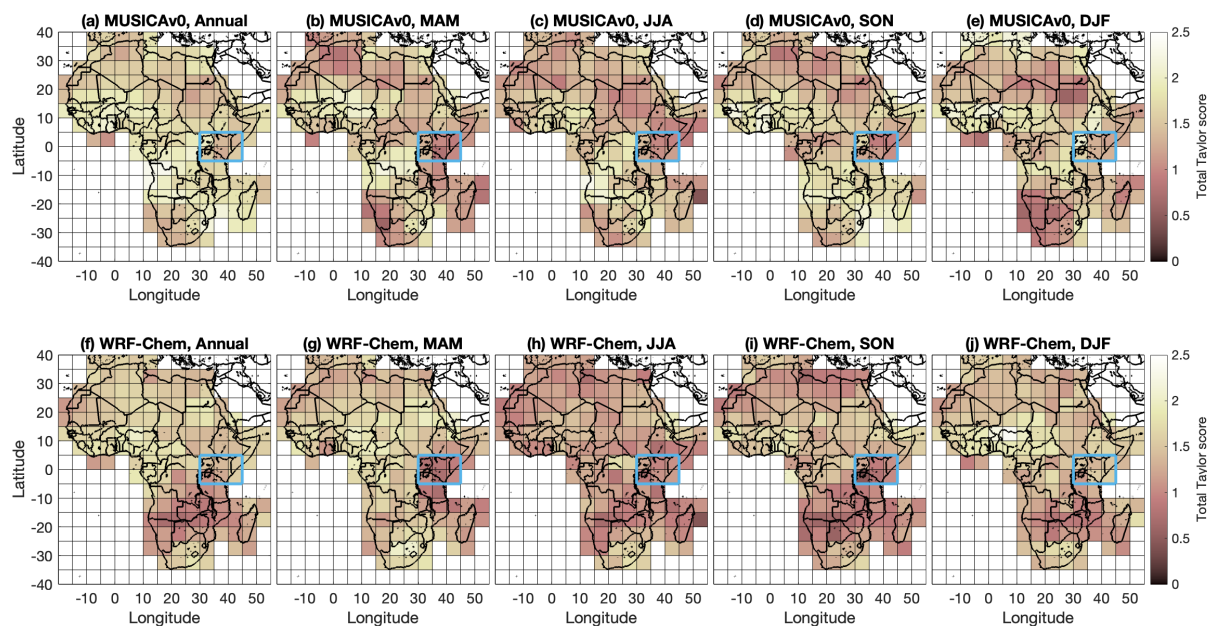


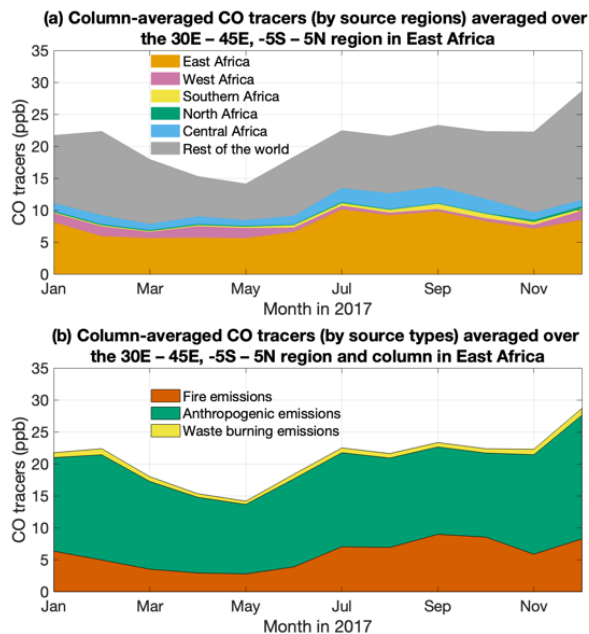
Figure 13. Same as Figure 9 but for over the Pacific Ocean.

1308
 1309
 1310
 1311
 1312
 1313



1314
 1315 **Figure 14.** Spatial distribution of total Taylor score of MUSICA v0 and (f-j) WRF-Chem compared
 1316 to satellite retrievals. In each $5^\circ \times 5^\circ$ (latitude \times longitude) pixel, Taylor scores of the model
 1317 compared to three satellite products (e.g., MOPITT CO column retrievals, OMI tropospheric NO₂
 1318 column retrievals, and MODIS AOD) are calculated separately (as shown in Figure S12). Taylor
 1319 score against each satellite product ranges from 0 to 1. And then three Taylor scores are summed
 1320 up to obtain the shown total Taylor score (ranges from 0 to 3). Total Taylor score of MUSICA v0
 1321 for (a) 2017, (b) MAM (March, April, and May), (c) JJA (June, July, and August), (d) SON
 1322 (September, October, and November), and (e) DJF (December, January, and February) are shown.
 1323 The blue box highlights a potential region for future field campaigns and/or in situ observations.
 1324 (f-j) are similar to (a-e) except for WRF-Chem.

1325
 1326
 1327



1328
 1329 **Figure 15.** Monthly time series of column-averaged CO tracers in the 30°E – 45°E, -5°S – 5°N
 1330 region in East Africa. (a) CO tracers of emissions from North Africa (green), West Africa (pink),
 1331 East Africa (orange), Central Africa (blue), Southern Africa (yellow), and the rest of the world
 1332 (grey). (b) CO tracers of fire emissions (red), anthropogenic emissions (green), and waste burning
 1333 emissions (yellow).

1334